Master's Thesis

LES of Turbulent Premixed Flame Kernel Formation and Development

Supervisor:
Dr. Suresh Menon

Author:
Alexander Lambert

Committee Member
Dr. Jeff Jagoda

Committee Member
Dr. Jerry Seitzman

May 7, 2013

Contents

List of Figures

List of Tables

1 Introduction

The combustion processes used in many common engineering applications typically take place in turbulent environments. Propulsion systems, such as jet and IC-engines, as well as gas turbines used for power generation, make use of turbulence to enhance mixing in their combustors and increase the rate of fuel burning. In order to start the burning process, many of these systems use forced ignition to introduce a sudden input of energy to the fuel/oxidizer and initiate the chemical reactions needed to sustain combustion. The most prevalent form of forced ignition is spark ignition, owing to its long-standing use in the internal combustion engine developed by the automotive industry. Igniting a flammable mixture and developing a stable, self-propagating flame is a highly transient process which is also sensitive to local conditions, such as turbulence levels. This can have a direct impact on the overall performance of the combustion system. Due to recent increase in governmental regulations aimed at reducing emissions, as well as the current economic climate, there is much interest in improving the efficiency and reliability of hydrocarbon-burning engines. There is then much practical importance in understanding how turbulence might affect the dynamics of spark ignition and subsequent flame development. In order to investigate this phenomenon, computational simulations possess the means to potentially capture and study in detail the relevant physics that are at play.

2 Background

2.1 Spark Ignition

The ignition of a flammable mixture encapsulates the process where the amount of energy added to the mixture crosses some critical threshold, and initiates a chain of chemical reactions. These chemical pathways are quite complex for hydrocarbon fuels, and involve steps

which can either add to or detract from the continuation of the mechanism. The buildup of key radicals can promote chain propagation, and can lead to the occurrence of a sudden exponential rise in heat-release, which typically characterizes an ignition event (as shown in Fig.2.1). This may or may not develop into a stable, self-sustaining flame depending on local conditions such as the levels of hydrodynamic strain, as well as the presence of walls which can introduce heat-losses. It is important to note the difference between such local ignition, and what some call "system ignition". The latter usually refers to the moment at which the initiated flame has stabilized in a given combustor geometry due to a balance in flame propagation and convective flow velocities.

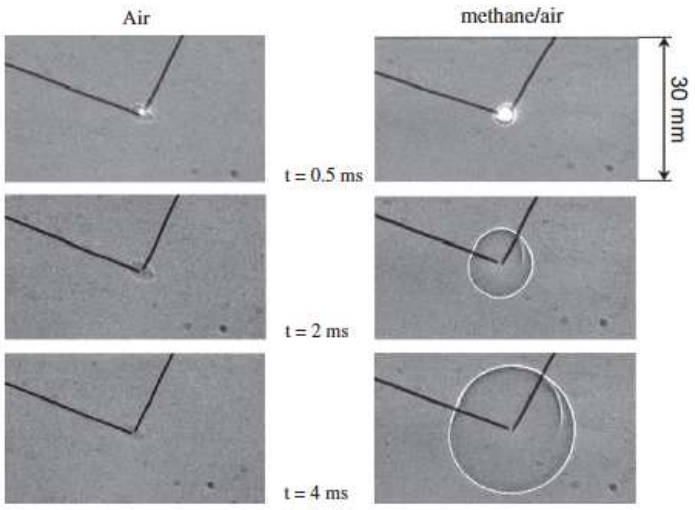

Fig. 1: Snapshots of sparks in air and stoichiometric CH_4/air mixture. A spherical flame develops in the fuel mixture following ignition [10].

In this respect, the process of spark ignition in particular can be defined as consisting of three main stages: (1) energy deposition by a spark discharge, (2) ignition and development of a flame kernel, and (3) propagation of a self-sustaining flame. The spark formation in the first stage begins with an applied voltage across a cathode-anode electrode pair separated by a gaseous medium. If the voltage is sufficiently high, molecules within the gas will become ionized (turning into a plasma) and produce free electrons, which in turn will be rapidly accelerated by the electric field and collide with other molecules, releasing more electrons. This is the breakdown process which produces an electric arc and establishes a current across the

electrodes, all taking place on the order of $1 - 10\eta s$. Extending past this time-frame is the energy that is deposited into the gas molecules due to collisions processes, and depending on the pulse width can last anywhere from micro- to milliseconds. Since the relaxation timescale of the different energy modes (translational, rotational, vibrational, electronic) are on the order of $1\eta s$, the gas past this stage is typically in thermal-equilibrium, allowing for temperatures on the order of thousands of Kelvin to be generated near the electrode tips [29, 35]. This differs from other forms of plasma discharges, which produce thermally non-equilibrium, low-temperature plasma and have recently attracted investigation into their potential uses in combustion and ignition [36]. This present study will focus primarily on equilibrium/spark plasma as a thermal ignition source, which is the type seen in most currently available applications.

This leads to the second stage, namely the formation of a flame kernel. The sudden rise in thermal energy produced by the spark causes the creation of a blast wave which propagates outwards from the spark origin. This initial expansion causes the temperature to drop within the heated region, allowing much of the energy from ionization to be converted back into thermal energy [29, 28, 27]. Generally, the kernel growth velocities decrease monotonically after spark energy deposition. However, it has been shown in experiment that the overpressure generated by the initial high pressure wave is the main cause of kernel expansion for the first $100\mu s$. Although there is a large degree of strain imposed on the flame due to rapid initial expansion, it has been suggested that the energy of the spark is typically sufficient to promote smaller chemical timescales and possibly a surplus of radicals, allowing the flame kernel to survive [5]. As the effect of pressure-driven expansion dissipates, kernel velocities slow down even faster and growth becomes principally driven by heat conduction and mass diffusion. In methane/air mixtures, the combustion chemistry can begin to enhance the growth of the flame as early as $1 - 10\mu s$ due to additional heat release, but only gradually begins to prevent deceleration of the flame front near $1ms$. The separation of the shockwave from the flame kernel, as well as the incremental effect of heat release with time is well illustrated in Fig.2.1. Eventually, the outward velocities converge to the laminar burning velocity [29, 5].

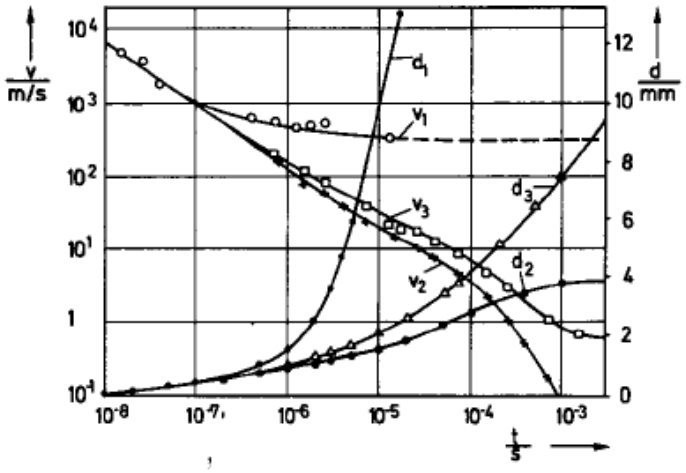

Fig. 2: Expansion velocities (v) and flame diameters (d) over time. Indicated are observed trends for the shock (1), plasma in air (2), and flame in CH_4/air ($\Phi = 1$) as measured by laser interferometry [29].

Studying the initial stages of the spark ignition process has been a significant challenge, where the timescales involved have made it extremely difficult to experimentally measure the chemical dynamics. Although the energy modes may be at thermal equilibrium for the case of spark deposition, it is uncertain to what extent the production of key combustion species, such as O and H radicals, is affected by the spark. The problem maybe be studied numerically, but in order to fully model the ignition process, one would have to take into account the magnetohydrodynamic effects of the electric field generated between the electrodes, include the changes in conductivity, and solve for the governing equations of plasma species which require ionized chemistry and transport properties. Implementing and solving such a system of equations would be non-trivial, particularly if it is to be coupled with a three-dimensional CFD solver which may include turbulence and combustion closures. Many previous studies which have conducted LES simulations of forced ignition in larger systems (such as IC engines, swirl and rocket combustors) have simply modeled the spark by including an energy deposition term in the energy equation, which follows a specific profile. This has generated surprisingly accurate results compared to experiment [26, 25, 17]. Moreover, it has been shown that the inclusion of ionized air chemistry in numerically modelling spark ignition causes higher concentrations of radicals during the first $10\mu s$ (ex. 3% peak mole-fraction of O with ionized

species versus 2% without) [38, 24]. This causes a difference in average temperature profile of approximately 100K for at least $25\mu s$. It is unclear exactly how such initial differences affect the ignition and combustion processes.

2.2 Spherical Flames & Flame Speeds

It has been shown by many experimental and numerical studies that the kernel shape depends strongly on the geometry of the igniter, where characteristics such as electrode diameter, shape, and gap width can directly affect the growth of the kernel [35, 28, 42]. The gap size in an opposing electrode geometry, for instance, can cause the flame kernel to expand more in the transverse direction and assume a toroidal shape, instead of becoming spherical [27, 22]. Despite this dependence, the spark can quickly assume a spherical shape provided the initial mixture conditions are quiescent and the spark electrodes are small enough, and the gap size sufficiently large, so as to prevent significant deformation [10, 8, 38]. An example of this is shown in Fig.2.2, where the electrodes affect the local flame velocity, possibly by inducing strain on flame propagation and/or through heat losses due to conduction [8].

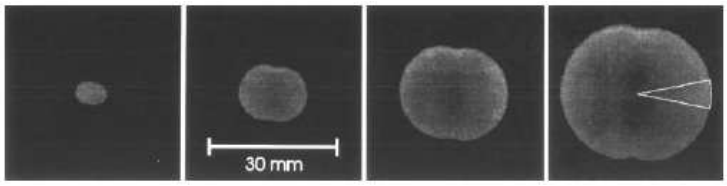

Fig. 3: Sequence of PLIF images following a a single spark ignition event in quiescent mixture. The intensities correspond to OH concentrations. The snapshots correspond to a range from 1.35 to 7.35ms, each separated by 2ms. The top and bottom indentations correspond to the electrode positions [8].

Many numerical studies have used this assumption as a justification for studying spherical flames [18]. Here, the starting point of the simulation is assumed to be the point in time after ignition where the kernel has recently acquired a fully developed flame front and is expanding outward into the quiescent unburned reactants solely due to mass diffusion and heat conduction. Although the spherical flame front is laminar, there are still expected differences in flame structure and flame speed compared to a planar laminar flame. This is due to the flame stretch imposed by the curvature of the flame front. Generally, flame stretch

is defined as the normalized rate of change in surface area of a surface element on the flame front:

$$\kappa = \frac{1}{A}\frac{dA}{dt} \tag{1}$$

For a thin flame sheet, the stretch can be derived as a function of the flame surface normal ($\vec{n}$), the flame displacement speed (S_d) and the local flow velocity ($\vec{u}$).

$$\kappa = -\vec{n}\vec{n} : \nabla\vec{u} + \nabla\vec{u} + S_d\nabla\cdot\vec{n} \tag{2}$$

The first term is the negative tensor of the velocity gradient normal to the flame surface, and second accounts for the general velocity gradient. The two first terms combined effectively represent the tangential strain rate acting parallel to the flame surface. The third and last term accounts for stretch due to flame curvature. Writing the equation in terms of the flame-normal coordinate system:

$$\kappa = \nabla_t\vec{u} + S_d\nabla_t\cdot\vec{n} \tag{3}$$

where $\nabla_t\vec{u}$ is now the tangential strain rate.

The flame displacement speed, S_d, is defined as the speed of the flame front relative to the local flame velocity.

$$S_d = \vec{w}\cdot\vec{n} - \vec{u}\cdot\vec{n} \tag{4}$$

where $\vec{w}$ is the absolute flame velocity. A surface of the flame front can be defined as the iso-level of a particular value of the reduced temperature, $\theta = \frac{T-T_u}{T_b-T_u}$. The displacement speed can then be written as a function of θ:

$$S_d = \vec{w}\cdot\vec{n} - \vec{u}\cdot\vec{n} = \frac{1}{|\nabla\theta|}\frac{\partial\theta}{\partial t} + \vec{u}\frac{\nabla\theta}{|\nabla\theta|} = \frac{1}{|\nabla\theta|}\frac{D\theta}{Dt} \tag{5}$$

where the operator $\frac{D}{Dt}$ is the material derivative. It is apparent that S_d is a local measure,

and will vary according to the value of θ it is associated to. Another useful definition is the consumption speed (S_c), which is a measure of the global fuel consumption.

$$S_c = -\frac{1}{\rho_u Y_f^u} \dot{\omega}_f dV \tag{6}$$

where ρ_u is the unburned mixture density, Y_f^u the unburned fuel mass fraction, and $\dot{\omega}_f$ the fuel reaction in rate. This is inherently a global parameter, as the reaction rate is integrated over the entire domain volume.

For a one-dimensional, unstretched laminar flame at standard temperature and pressure ($T^0 = 298\text{K}, P^0 = 101.3\text{kPa}$), the laminar flame speed (S_L) is set as the nominal reference value (S_L^0). This value is constant throughout the domain, as all iso-surfaces travel in parallel if the flame fully developed. The consumption speed in this case is equal to the laminar flame speed ($S_c = S_L^0$), whereas the displacement speed is dependent on the local density ($S_d = \frac{\rho}{\rho_u} S_L^0$), which differs across the flame front.

A spherical laminar flame will undergo stretch due to the curvature associated with its shape, and will therefore be determined by the second term in eq. 3. This can also be easily derived from the instantaneous flame surface area ($A = 4\pi r(t)^2$):

$$\kappa = \frac{1}{A}\frac{dA}{dt} = \frac{2}{r(t)}\frac{d}{dt} r(t) \tag{7}$$

where $r(t)$ is the radius of the flame front as a function of time. Assuming an infinitely thin flame front, the flame speeds can be derived to be:

$$S_c = \frac{\rho_b}{\rho_u}\frac{d}{dt} r(t) = S_d \tag{8}$$

where ρ_b is the density of the burned mixture or products. In this theoretical idealization, S_d is equal to S_c. Obviously, this is not exactly the case in realistic flame with finite thickness. However, the first-order approximation gives us an expected linear relationship between the

consumption speed S_c and radial velocity, the latter of which is relatively easy to measure in experiment. The flow velocity profile through the flame can also be derived under the the same assumptions. The flow speed within the sphere of burnt gas must be zero in order to conserve mass in the closed region of uniform density while the system is at constant pressure. Beyond the flame front, however, the mass flux through a spherical area of radius R will be outward in order to compensate for the decrease in mass within this spherical volume due to the expanding burnt region of low-density products.

$$u(R) = \left(\frac{r(t)}{R}\right)^2 \left(1 - \frac{\rho_u}{\rho_b}\right) \frac{d}{dt} r(t) \tag{9}$$

This shows that the instantaneous flow velocity decreases monotonically as the outward distance from the flame front increases.

The flame stretch due to curvature decreases monotonically with time, since it is directly related to the inverse of the radius. This results in a similar trend in flame thickness, which is initially much thicker at a radius only an order of magnitude larger than the laminar flame thickness. However, the thickness decreases quickly with radius and converges to the laminar value. An inverse relation is present between the absolute flame propagation speed with radius, where it increases quite rapidly initially, then slowly converges to the laminar flame speed. This has been confirmed by both experimental and numerical experiments, as exemplified by Fig.2.2.

2.3 Turbulent Combustion

The effects of turbulence on the combustion process take shape principally through alteration of the flame structure, which may increase the rate of burning or lower it, and possibly quench it altogether. However, heat release from combustion can affect turbulence by inducing flow accelerations as well as increasing the kinematic viscosity, which dampens turbulent fluctuations. The coupling taking place in turbulent combustion can therefore lead to very different

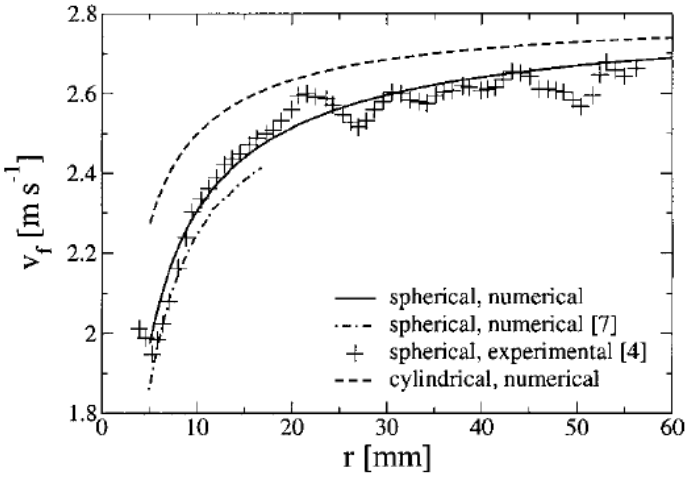

Fig. 4: Numerical and experimental results of flame propagation velocity v_f for spherically (and cylindrically) expanding flames at the 305K iso-level. The oscillations in the experimental data correspond to acoustic perturbations [19, 18].

flame behavior depending on the conditions of the system.

Studying the physics of premixed turbulent combustion essentially comprises of a comparison in length and timescales between the mechanical fluid motions and the combustion chemistry. This determines to what extent one process might influence another, and which is the dominant factor in governing flame dynamics. In this regard, there are some key parameters which are essential to the discussion.

$$\tau_{flow} = \text{characteristic flow time} = \frac{\ell_t}{u'} \tag{10}$$

$$\tau_k = \text{characteristic flow time at the Kolmogorov lengthscale} = \frac{\eta_k}{u'_k} \tag{11}$$

$$\tau_{chem} = \text{characteristic chemical time} = \frac{\delta}{S_L} \tag{12}$$

where ℓ_t is the integral lengthscale, u' the integral RMS velocity, η_k the Kolmogorov lengthscale, u'_k the velocity at η_k, δ the laminar flame thickness and S_L the laminar flame speed. These timescales can be compared to each other in order to define certain non-

dimensional parameters:

- Damköhler number (Da):

$$Da \equiv \frac{\tau_{flow}}{\tau_{chem}} = \frac{\ell_t/u'}{\delta/S_L} = \left(\frac{\ell_t}{\delta}\right)\left(\frac{u'}{S_L}\right)^{-1} \tag{13}$$

- Karlovitz number (Ka):

$$Ka \equiv \frac{\tau_{chem}}{\tau_k} = \frac{u'_k/\eta_k}{S_L/\delta} \tag{14}$$

  Using relations for the turbulent dissipation and turbulent Reynolds number Re_t, this may also be written as

$$Ka = \left(\frac{l_0}{\delta}\right)^{-1/2}\left(\frac{u'}{S_L}\right)^{3/2} = \left(\frac{\delta}{\eta_k}\right)^2 \tag{15}$$

Comparing the different values of timescales has led to the categorization of premixed turbulent flames into different regimes, as it is traditionally represented in the Borghi diagram (Fig.2.3). In the "flamelet regime", the chemical timescales are smaller than any turbulent timescale ($Ka < 1$), and the flame front can be approximated as being composed of many individual laminar planar surfaces, or 'flamelets', each propagating locally at a the laminar flame speed S_L. However, the turbulent motions can still wrinkle the flame front surface, and if $u' > S_L$, interactions between flame fronts and pockets of burned and unburned gases may be observed (this is the "corrugated flamelet regime"). If the chemical timescale is less than the integral turbulent timescale, but greater than the Kolmogrov timescale (corresponding to $Ka > 1$ and $Da > 1$), the smaller eddies are then able to penetrate the flame front, thickening it in the process, hence the name "thickened flame regime". If $Da < 1$, then all turbulent eddies have characteristic times shorter than the chemical time, allowing for fast mixing and simulating a "well-stirred reactor". Peters [30] later modified the diagram to take into account the different lengthscales associated with the preheat and reaction zone portions of the flame front (Fig.2.3). As before, an increase of Ka over unity implies that turbulent motions are able to affect the flame front. However, if $Ka < 100$, only the preheat zone is affected and subsequently thickened. This is called the "thin reaction zone regime" (TRZ). If $Ka > 100$,

the flame front is said to be in the "broken reaction zone regime" (BRZ) as the reaction zone can then be perturbed by turbulent eddies, which may lead to local extinction and reignition. It should be stressed that the values marking these transitions are order-of-magnitude estimates, and is approximated for a planar, fully-developed flame front.

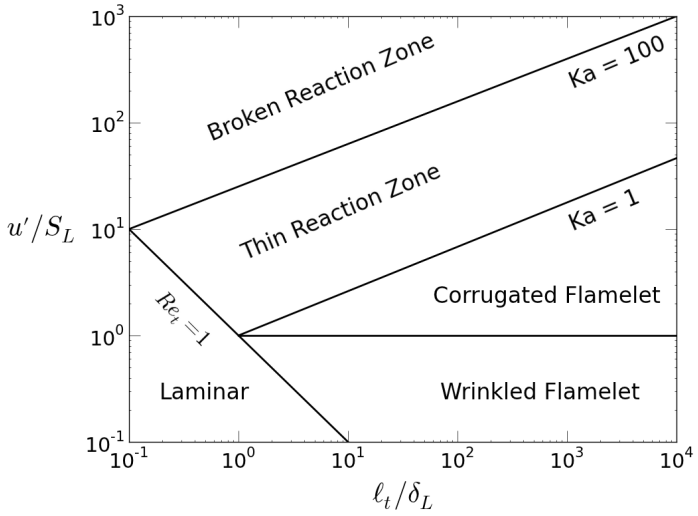

Fig. 5: Borghi diagram as modified by Peters [30].

A main measure of flame propagation in a turbulent mixture is the turbulent flame speed, S_T, which is greater than the laminar flame speed S_L. In the flamelet regime, S_T increases roughly linearly with u'/S_L. This is due to the wrinkling and distortion of the flame front by turbulent motions, which effectively increases the total flame surface area. The turbulent surface area A_T of a planar flamesheet would then be larger than the the area of the unperturbed flame (A_L) of the same projectional surface area in the direction of flame propagation. An increase in surface area raises the overall rate of fuel consumption and heat release. Turbulent scales larger than the flame thickness ($\ell > \delta$) can also induce stretch, which will also affect S_T.

It is worth pointing out that the the effects produced by turbulent wrinkling at one moment in time may be felt by the flame much later on. For instance, a particularly high-energy eddy may cause the flame to acquire a large "dent" of significant curvature at one location of its surface. Even as the turbulence dissipates and no longer contains any eddies of similar

strength, the topology of the flame may still remain warped to some degree by the earlier deformation. Subsequent flame growth, as in the spherical case, may actually accentuate the distortion [9, 41].

2.4 Sparks in Turbulent Mixtures

It has been known for some time that igniting a spark requires more energy when the mixture is turbulent [7, 3, 2]. This is manifested through the additional hydrodynamic strain rate accompanying the turbulent motions. If the characteristic turbulent timescale ℓ_t/u' is greater than the characteristic chemical timescale, the flame kernel will quench [1]. As mentioned earlier, the kernel expansion during the first $100\mu s$ is mainly governed by the pressure and thermal gradients which follow the initial shock wave. This is followed by a regime of spark-assisted propagation, in which the residual thermal energy and radical concentrations enabled by the spark allows the flame to survive the initial high strain rates which accompany the deposition of a given spark energy. This effect persists even after the spark has ceased [5]. For the turbulent case, strong velocity fluctuations can contribute additional hydrodynamic strain during the initial rapid expansion phase and quench the kernel before it has formed a self-sustaining flame front. If the turbulent levels are insufficient to compete against the thermochemical "boost" given by the spark, they may still quench the flame once enough spark energy has dissipated (as shown in Fig.2.4 [2]. For turbulent intensities which represent practical operation conditions in many common systems (where $Da \ll 1$), the turbulent timescales are too large to compare to the reduced chemical timescales during spark-assisted propagation. There is thus a time delay seen from the end of the spark to the moment which turbulence begins to affect flame propagation. This has been shown to vary on the order of $100\mu s$. If turbulence levels are sufficiently high, there may be statistical variation on whether the flame kernel grows enough to propagate continuously, or quench due to combined turbulent and spherical strain. This is reflected in the work performed by Eyssartier et. al. [13], where the spark-ignition of a laboratory-scale swirl combustor was simulated. Although this involved multi-phase combustion of kerosene spray, distinct stages of the turbulent ignition process can be seen in Fig.2.4: an initial rapid rise in fuel consumption (or decomposition)

due to the spark, followed by a collapsed region of laminar combustion, followed by variant turbulent flame speeds.

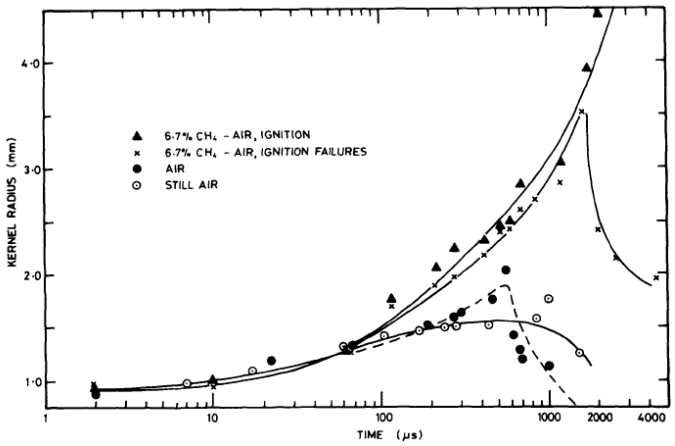

Fig. 6: Average spherical radius versus time for propagating/quenched flames and quiescent/turbulent air plasma at characteristic turbulent time of $\ell_t/u' = 8.3$ms [2].

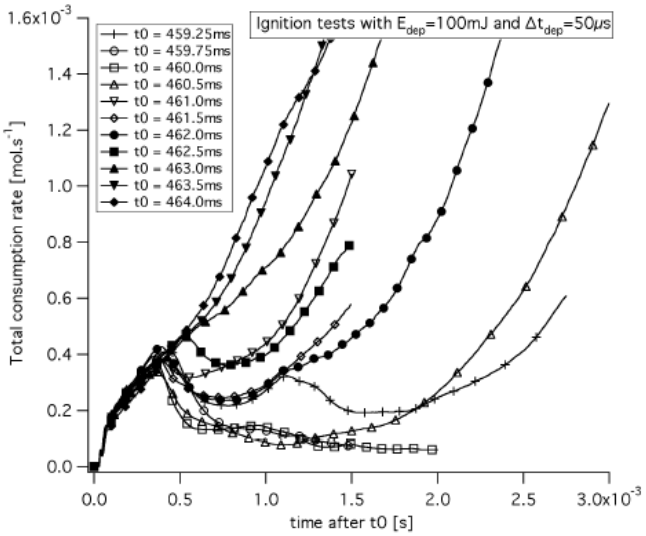

Fig. 7: Time evolution of total consumption rate ($\int \dot{w} dV$) for multiple successive spark ignition attempts, where t_0 is the sparking time [13].

2.5 Turbulent Spherical Flames

The time delay often seen in turbulent spark ignition is supportive of the initialization assumption made in many numerical studies of spherical flames. It is reasoned that the simulation

can begin with a spherical laminar flame which approximates the true flame structure the moment before it starts being affected by turbulent motions [20, 37, 6, 14]. The kernel shapes and flame propagation values resulting from these computational endeavors generally appear to match fairly well with experimental data extracted from imaging diagnostics (OH-PLIF, high-speed photography)[15, 41]. This is used as justification by computational studies of spherical flames to avoid having to model the ignition process and the formation of the flame kernel itself. An example of such a simulation is shown in Fig.2.5, where a spherical laminar flame is initially super-imposed on a freely-decaying, isotropic turbulent field and allowed to develop.

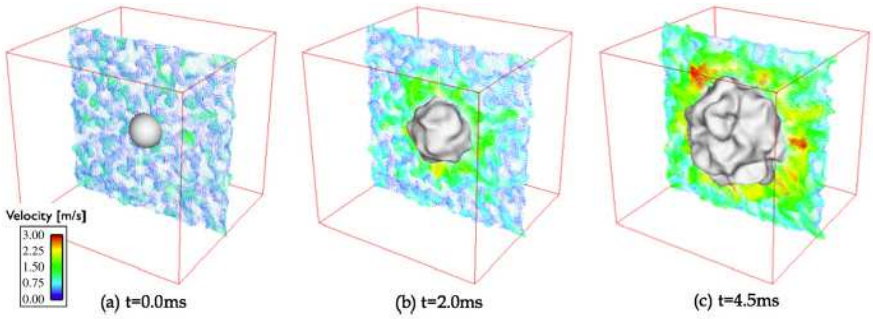

Fig. 8: Iso-surfaces for the filtered progress variable value of $\tilde{c} = 0.5$ with velocity vectors colored by velocity magnitude in the $x = 0$ plane [41].

As with statistically planar flames, the relation to curvature will vary depending on the Lewis number. If Le$<$ 1, molecular diffusion of reactants is greater than the thermal diffusivity. This will increase S_L if the flame is positively curved, and decrease S_L for negative curvature. The net effect is an amplification of curvature, which will make the flame much more sensitive to perturbations and more prone to local extinction. For Le$>$ 1, molecular diffusion is less than the thermal diffusivity, and the inverse relation applies. Here, the flame will have a propensity for self-stabilization, where local diffusive fluxes counteract the effects of flow-induced curvature and may result in a reduction of local flame speeds. These thermodiffusive instabilities similarly occur in turbulent spherical flames, as demonstrated experimentally by Renou et. al. [31]. Here, the authors chose to compare spherically flame behavior to turbulence for mixtures with different fuels, and therefore different Lewis num-

bers. The selected fuels were propane (Le$>$ 1), methane (Le $\approx$ 1) and hydrogen (Le$<$ 1), and were mixed with air at different equivalence ratios to obtain similar resulting flame speeds: $\Phi_{CH_4} = \Phi_{C_3H_8} = 1$ and $\Phi_{H_2} = 0.27$. The turbulent intensities were selected in a range of $u' = 0 - 0.51$ such that the resulting turbulent flames operated within the flamelet regime (Ka$<$ 1). The flame kernels in this were allowed to develop in freely-decaying isotropic turbulence. The resulting flame fronts were captured using a high-speed camera, allowing the 2D contours of the flame to be defined.

Under the assumption of an infinitely thin flame-front, the two-dimensional local curvatures were calculated and averaged over the flame images to obtain a mean curvature $\langle h \rangle$. Incorporating both negative and positive flame curvatures together, the resulting $\langle h \rangle$ value should be similar to $1/\langle R \rangle$ where $\langle R \rangle$ is the mean flame radius. To better represent the fluctuations in wrinkling, the rms curvature h_{rms} was also calculated. As seen in Fig. 10, the $\langle h \rangle$ values for all flames tended towards zero as the kernels grew. However, there were differences observed between the fuel mixtures, where propane appeared to decrease the slowest. Looking at the h_{rms} distributions, it was seen that the curvature values were generally greater for C_3H_8 (Le= 1.40) compared to CH_4, and even more so for H_2 (Le=0.33). Therefore, there was a clear difference in response to the same level of turbulence when considering the observed flame front wrinkling. Though, it seems surprising that the level of curvature measured in the propane mixture is greater than that in the methane. According to the theory, one would expect that the counteracting thermodiffusive effects of the propane fuel would tend to suppress local curvature, which would result in less wrinkling.

Despite the observed difference in curvature values, the flame displacement speed S_d measurements did not appear to follow the same trend. The authors also calculated both the mean ($\langle S_d \rangle$) and rms ($\langle S_d \rangle$) displacement speed. As shown in Fig. 11a, the results indicated that all flame speeds converged to their respective planar laminar flame speeds as the kernels grew in size, which was due to the diminishing effect of the mean curvature imposed by the spherical shape. The hydrogen flame speed seem to differ much more from its planar

value compared to methane and propane, indicating a larger sensitivity to stretch. This is also apparent in the stretch imposed by turbulence (Fig. 11b), where the fluctuations actually increase in the H_2 case over time and indicative of the species' stretch-enhancing behavior.

A crucial result for the purposes of this discussion is that the turbulent flame speeds for both CH_4 and C_3H_8 mixtures were found to be very similar. Given the differences in the observed curvature, the finding suggests that the net effect of turbulence on both of these flames is the same. Taking into account the results for the H_2 case, this is also supportive of the conclusion that the influence of Lewis number on flame speeds is heavily non-linear.

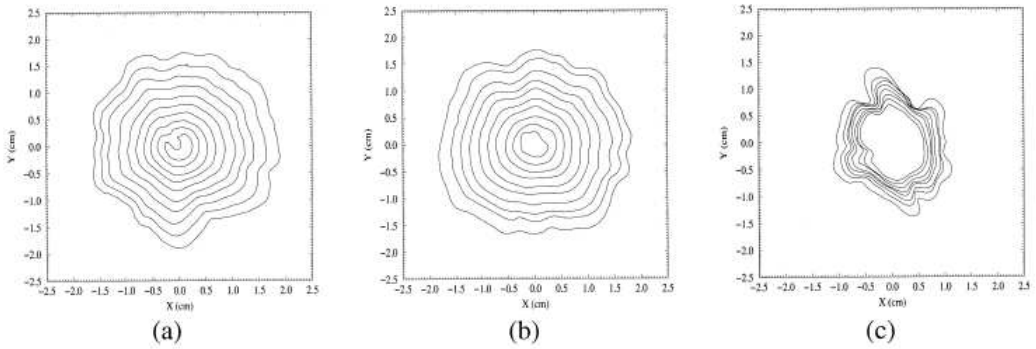

Fig. 9: Flame front contour evolution at different times (growing outwards) for different fuel/air mixtures at $u' = 0.18$: (a) C_3H_8, (b) CH_4, (c) H_2. Taken from experiment [31].

The use of DNS to study spherical flame interaction with isotropic turbulence allows all the relevant lengthscales in the problem to be resolved, which captures the larger corrugative effects as well as changes to the flame front internal structure. This is particularly useful at higher turbulence levels where turbulent scales are small enough to penetrate the flame front, such as within the TRZ and BRZ regimes. The computational cost of carrying out DNS simulations, however, is often very prohibitive. Only recently has full 3D DNS of spherical turbulent flames been performed [15, 37, 14]. It will be some length of time before such an approach can be used on larger-scale turbulent flames in more practical configurations. Modelling certain aspects of the turbulent flame behavior would help lower these costs, which is why the potential of LES makes it an attractive candidate for performing accurate simulations

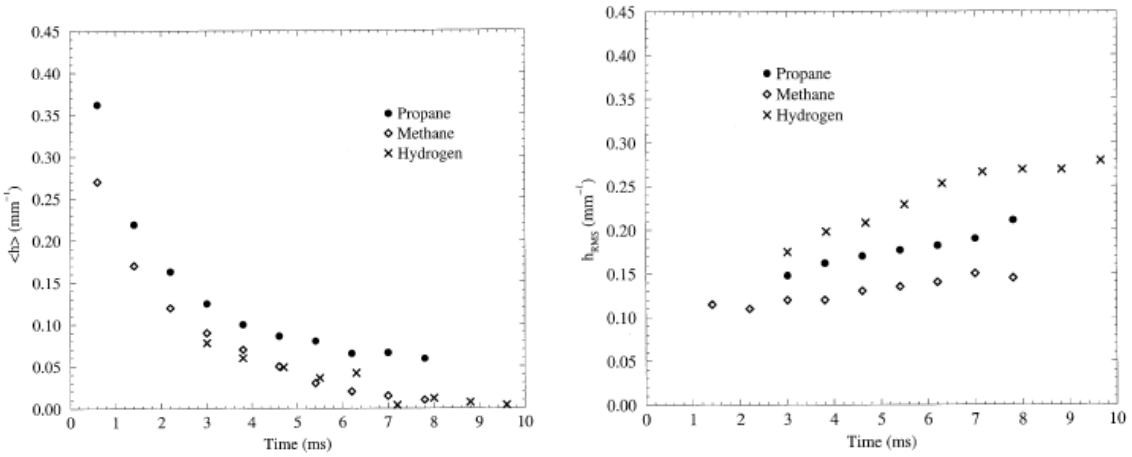

Fig. 10: Temporal evolution of (a) mean curvature and (b) RMS curvature for mixtures of CH_4/air ($\Phi = 1$), C_3H_8/air ($\Phi = 1.0$), and H_2/air ($\Phi = 1.0$) at $u'(t = 0) = 0.34$m/s [31].

of spherical turbulent flames in more commercially-oriented geometries. However, before a given LES method or closure can be applied for use at larger scales, it is common practice to ensure its applicability by first testing it for similar operating regimes in a reduced, more fundamental configuration. This can then be tested both against experiment and high-resolution LES or DNS.

There has recently been interest in developing models for turbulence-induced flame wrinkling for use as an LES closure [12, 32, 40] . This approach attempts to take into account the degree of flame wrinkling by relating the flame-surface density (FSD) to the resolved turbulent flame characteristics. A recent study by Wang et. al. [41] employed an FSD-LES methodology to simulate the spherical propane flames in the aforementioned work by Renou et. al [31]. The simulations were carried out for both 2D and 3D using a single-step progress-variable chemistry calibrated for a stoichiometric propane mixture. They employed a unity Lewis number assumption, which was supported by the experimental results (as discussed earlier). The simulations for the 3D cases were carried out on a cubic domain 60mm in length, with a cartesian mesh 0.6mm in resolution.

The FSD subgrid model attempts to close the filtered reaction rate $\tilde{\omega}_c$ of the progress-

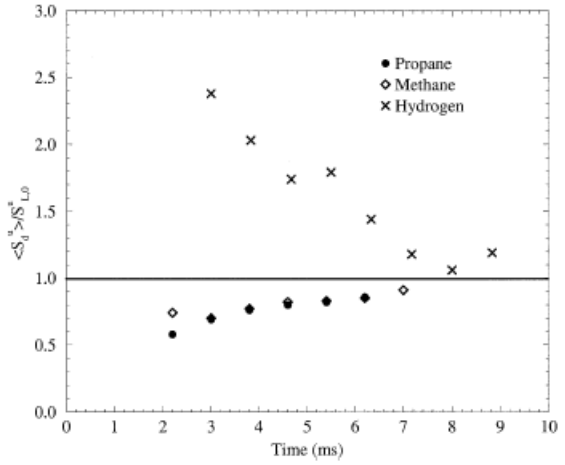

(a)

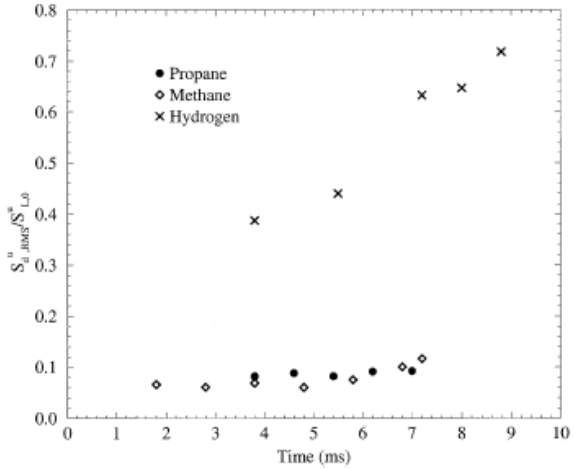

(b)

Fig. 11: Temporal evolution of (a) mean displacement speed and (b) RMS flame displacement speed for mixtures of CH_4/air ($\Phi = 1.0$), C_3H_8/air ($\Phi = 1.0$), and H_2/air ($\Phi = 0.27$) at $u'(t = 0) = 0.34$m/s [31].

variable c :

$$\tilde{\dot{\omega}}_c = \rho^u S_L^0 \Sigma \tag{16}$$

where ρ^u is the unburned reactant density, S_L^0 is the unstretched laminar flame speed and Σ is the flame surface density. The closure falls on relating Σ to the filtered reaction progress variable $\tilde{c}$:

$$\Sigma = 4\sqrt{\frac{6}{\pi}}\left(\frac{\Delta}{\delta_c}\right)^{\beta}\frac{\tilde{c}(1-\tilde{c})}{\Delta} \tag{17}$$

where Δ is the LES filter size, and δ_c represents the smallest scale of turbulent eddies which interact with the flame front. β is a dynamic model parameter which is dependent on the magnitude of the progress-variable gradient $|\nabla\tilde{c}|$ and filter size.

The authors compared their results to those of experimental reference using two definitions of flame radius. This was done first by computing the total flame surface area:

$$S_{tot}(t) = \int_V \Xi_\Delta |\nabla\tilde{c}| dv \tag{18}$$

where Ξ_Δ is the subgrid wrinkling factor and V indicates integration over the whole computational volume. The total flame radius R_p is then defined as the radius of the spherical flame having a total surface area of S_{tot}:

$$R_p(t) = \left(\frac{S_{tot}(t)}{4\pi}\right)^{1/2} \tag{19}$$

This term captures the increase in surface area due to the turbulent wrinkling as well as volumetric expansion. Furthermore, the total volume of burnt gases V_b was calculated is as:

$$V_b(t) = \int_V \tilde{c} dv \tag{20}$$

The mean flame radius R_s is then defined as that of the spherical flame having the same total volume of burned gas:

$$R_s(t) = \left(\frac{3V_b(t)}{4\pi}\right)^{1/3} \tag{21}$$

This is representative of the the average growth of the kernel due to the turbulent flame speed.

The authors managed to replicate the effect of wrinkling and corrugation on flame growth, as seen by the R_p and R_s distributions in Fig. 12. It was thus claimed that such an LES

approach can be used to correctly model turbulent spherical flames in this regime of premixed turbulent combustion.

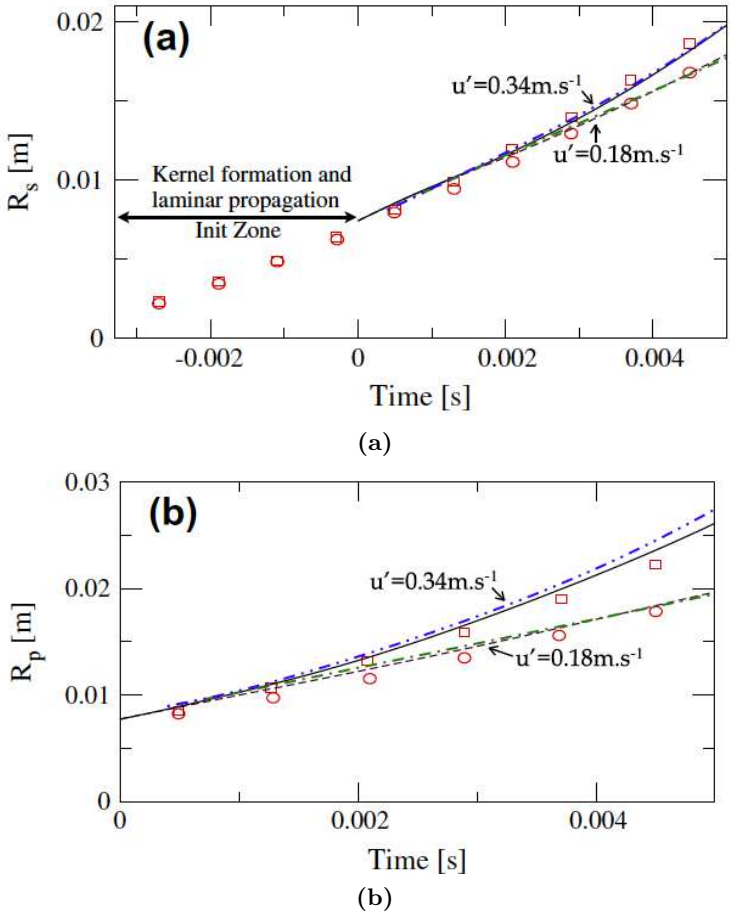

Fig. 12: Temporal evolution of the characteristic flame radii for (a) mean radius R_s and (b) total radius R_p. The symbols correspond to the experimental results from [31], where the squares are for $u' = 0.34$m/s and the circles for $u' = 0.18$m/s. The lines indicate the FSD-LES results from Wang et. al. [41], where the different colors represent the different LES filter sizes used.

Although the study seemed to be successful in replicating the experiment, it is surprising that such close agreement can be achieved using a cartesian grid for a spherical problem. One might expect a level of disparity between gradients which are normal to the global axes and those which are not, inducing a level of numerical dissipation which might possibly causing non-spherical growth of the flame. There is no indication of such an effect being accounted for in the LES closure used [41]. Furthermore, although characteristic outflow boundary con-

ditions were employed, the grid size is comparable to the size of the flame at times $t > 6$ms. The proximity to the boundaries may also be expected to produce some non-isotropic behavior. Vortical structures cannot be preserved at the boundaries since the velocities entering the domain are not properly accounted for. If turbulent scales are large (as they are in this problem, where $L_{11} = 5 - 10\%$ of the boundary dimension), then the spherical flame might deviate from the experiment as it approaches the boundaries.

With these possible issues in mind, it would be useful to compare the FSD-LES results to a more resolved simulation which does not employ the use of the FSD closure. This will ascertain whether the results are reproducible using a simplified by slightly more expensive computational approach. Additionally, it would verify whether the chosen geometry size and boundary conditions can be used to accurately simulate such operating conditions (such as turbulent scales, flame initialization, etc.). Such added validity would lend credence to the use of LES in simulating such a problem.

3 Objectives

1. Validate the use of an LES approach in simulating the spherical turbulent flame problem within the wrinkled flamelet regime.

   An LES simulation will be performed in order to test the use of a simplified LES closure for a turbulent spherical flame. It will be assumed that the flame front is locally laminar, where the internal structure of the flame is not affected by turbulent motions and is dependent solely on thermal and molecular diffusion. A turbulence-combustion closure will then not be necessary so long as the flame front gradients are adequately resolved. This will be compared to the FSD-LES results as well as experimental measurements from previous studies.

2. Simulate spark ignition in a practical configuration with mean flow velocity and determine the key physics governing the development of the ensuing flame kernel.

   The chosen system will consist of an opposing-electrode igniter centered in a rectangular

channel. The purposed effect of heightened initial radical concencentrations on resulting kernel development will be studied. Additionally both laminar and turbulent inflows will be compared to determine the differences caused by velocity fluctuations, and how these differences occur.

4 Numerical Setup

All simulations were performed using the fully-compressible, LESLIE code (**CITE LESLIE PAPERS**) for structured grids, where each employed different solver configurations to optimize performance and reliability.

4.1 Spherical Turbulent Flame

In order to test the chosen computational approach in simulating a post-spark spherical flame, a base-line validation study was performed using the results of Wang et. al. [41] and Renou et. al. [31]. Although their results were generated for relatively low turbulent levels ($u'_{max} = 0.54$m/s) with premixed combustion occurring in the flamelet regime, the two studies together form a good comparison between what has already been achieved both numerically and experimentally for this particular combustion problem.

4.1.1 Numerical Solver

The simulation was run using a second-order explicit MacCormack central-differencing scheme with second-order time integration. Since the cases involved in this portion of the study fell into the flamelet regime of turbulent combustion, the structure of the flame can be assumed to be laminar and would then not require a mixing model to include the effects of eddies entering the flame front. Instead of the FSD-LES model used by Wang. et. al., this study opted for a higher resolution to adequately capture flame wrinkling, as well as a using a Localized Dynamic Kinetic energy Model (LDKM) turbulence closure to model any unresolved fluxes that may be present. A thermally-perfect ideal gas was assumed, and the diffusive transport was calculated based on a mixture-averaged formulation.

4.1.2 Computational Grid & Boundary Conditions

The computational domain consisted of a simple cube geometry measuring 6.0cm on all sides, and contained a Cartesian grid with uniform cell spacing. This configuration was chosen to match the domain used by Wang et. al. However, since no subgrid-mixing closure was used for this preliminary study, a resolution of 0.23mm (256^3 grid points) was used instead of the 0.6mm resolution from the FSD-LES computation. In order to allow pressure fluctuations arising from the intialization to propagate out of the domain, each of the six sides of the domain were given a non-reflecting outflow subsonic boundary condition. Once the pressure waves had left, the boundary conditions were then set to supersonic outflows. This was necessary since the characteristic subsonic BC's induced numerical pressure spikes after some time for turbulent vortices at the boundaries. This formulation accounts for modal oscillations that are produced by acoustic fluctuations, and cannot converge on statistically stationary turbulence without mean velocity at the boundaries. The supersonic condition does not attempt to predict negative velocities relative to the boundaries, and therefore is much more lenient on numerical convergence. Although recirculating vortices will cause local pressure drops at the boundaries, the effects were restricted to regions within a few cells from the domain edges, and did not propagate into the main computational volume.

4.1.3 Chemistry

The combustion chemistry is modeled using Arrhenius type reaction rates in a reduced two-step C_3H_8/air chemical mechanism as described in [11]. The chemistry contains five species and is described by the following reactions:

$$C_3H_8 + 3.5O_2 \rightarrow 3CO + 3H_2O \tag{22}$$

$$CO + 0.5O_2 \rightleftharpoons CO_2 \tag{23}$$

The reaction coefficients were modified to match the flame speeds and species concentrations taken from experimental measurements [39, 4]. The mechanism was validated using a 1-D laminar flame configuration with the Cantera chemical kinetics calculator [16]. It is shown

in Fig.13a that the temperature profiles for a stoichiometric flame match the experiment even more closely than the GRI3.0 mechanism. The species profiles depicted in Fig.13b are also in reasonably good agreement with experiment. In order to justify the the resolution used in the full 3D simulation, the laminar profile was computed using the LESLIE code for a 1D grid with a resolution of 0.23mm (Fig. 13c). The resulting coarsened profile matches those on the fine 1D results quite well, indicating that the gradients are sufficiently resolved with such a resolution. The flamespeeds were also calculated for a range of equivalence ratios, and are shown to be approximately equivalent to the experimental values for lean and stoichiometric cases (Fig.14).

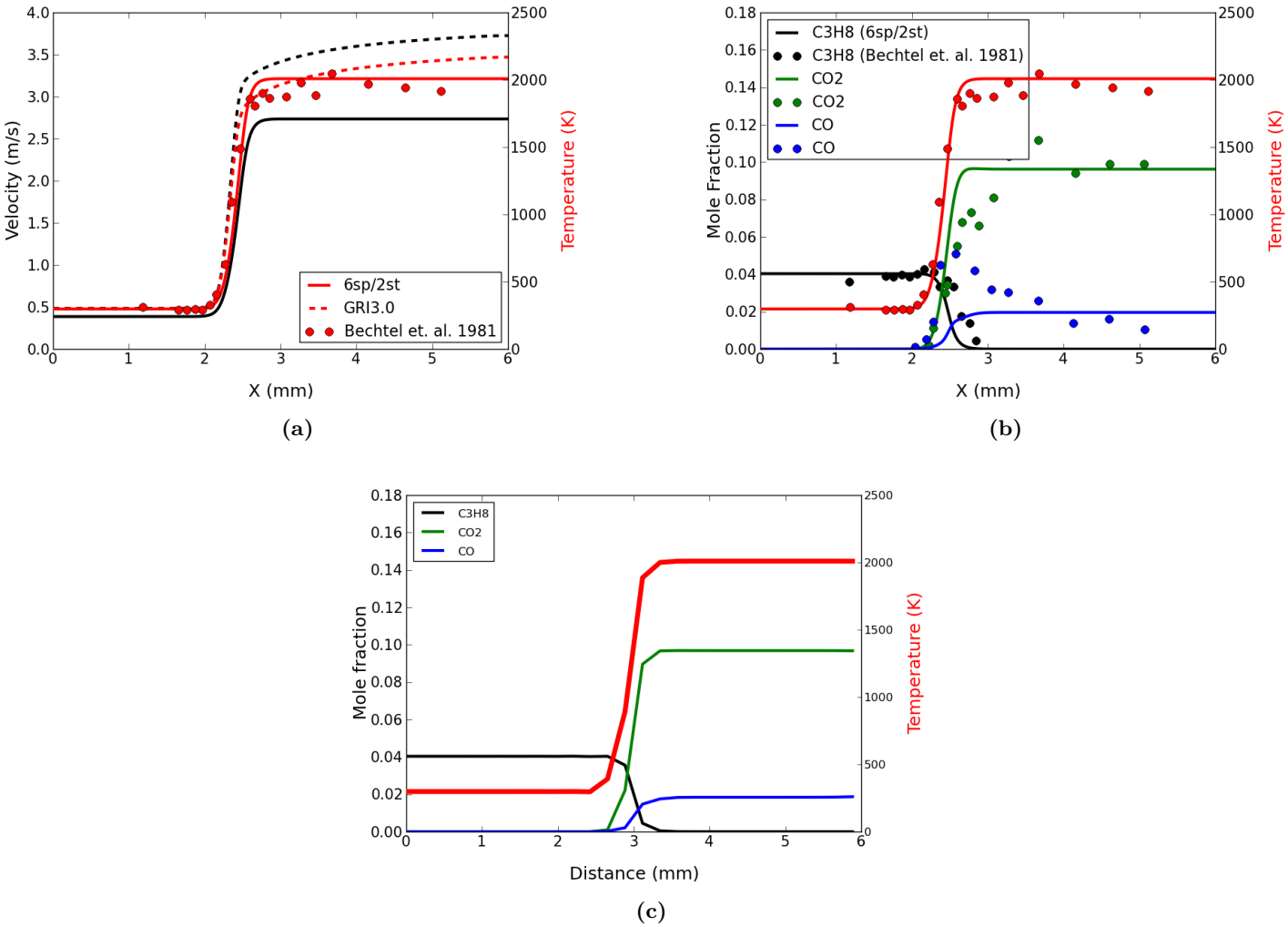

Fig. 13: Profiles of (a) velocity, temperature and (b) species mole fractions for a laminar flame. Comparisons are made between the 6-species/2-step C_3H_8 mechanism, GRImech3.0, and experiment [**?**]. Also shown are the (c) LESLIE profile results using a coarsened grid.

Fig. 14: Comparison of flamespeeds calculated using reduced mechanism, GRImech3.0, and those found in experiment [39].

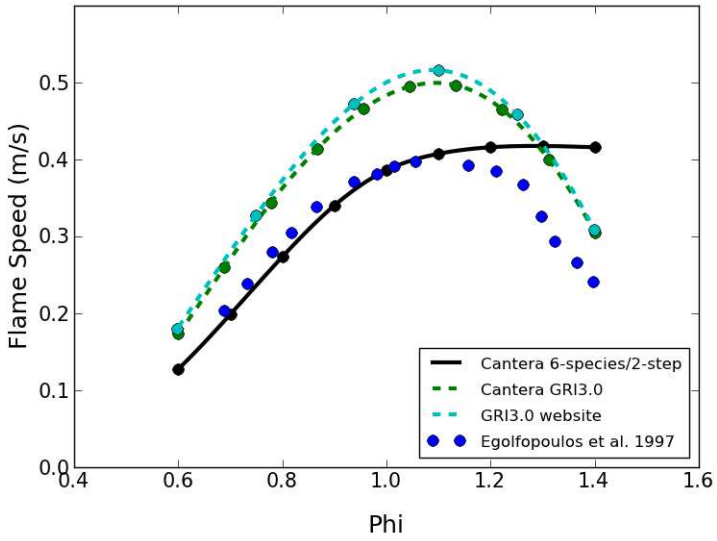

4.1.4 Initial Conditions

The cases selected for comparison contained stoichiometric mixtures of C_3H_8/air, as this was the fuel selected by the authors of the computational study in performing their own comparison to experiment. The simulations were carried out at a temperature of 300K and a pressure of 1 atm. Two different r.m.s velocities were used: $u' = 0.18$m/s (Case B) and $u' = 0.34m/s$ (Case C). The case names correspond to those found in [41]. The parameters used in the study, as well as those from the experiment, are summarized in Table 1 Before initializing the flame, measures were taken in order to acquire a statistically isotropic turbulent field. The turbulence was first produced using a Von-Karman Pao spectrum on a 512^3 point cubic grid with a resolution of 0.12mm, which was sufficient to resolve all eddy lengthscales. The turbulence was then run using DNS with a fourth-order accurate scheme and allowed to develop. The resulting solution was filtered onto a 256^3 point grid, where subgrid kinetic energies were calculated for the unresolved scales. This filtered solution was then developed further, this time performing LES using a LDKM subgrid closure. The turbulence decayed until the characteristic parameters were sufficiently close to the target values indicated in Renou et. al. (Table 1). This process allowed for accurate calculation of turbulent energies

at both resolved and unresolved scales. The resulting kinetic energy spectra are shown in Fig.15, where an inertial subrange can be seen in both cases.

Case	Source	u' (m/s)	L_{11} (mm)	η_k (mm)	δ_L (mm)	Φ	S_L (m/s)
B	Current study	0.17	2.58	0.145	0.105	1.0	0.386
—	Renou et. al.	0.18	3.0	0.21	0.100	1.0	0.407
C	Current study	0.33	6.38	0.13	0.105	1.0	0.386
—	Renou et. al.	0.34	6.5	0.16	0.100	1.0	0.407
	u'/S_L	Re_t	Re_λ	Da	Ka		
B	0.44	29	13.4	52	0.06		
—	0.44	36	—	68	0.05		
C	0.86	141	38.4	71	0.10		
—	0.84	146	—	78	0.09		

Table 1: Summary of case parameter settings for numerical simulations to be performed in the study in comparison to the experimental values from Renou et. al. . The flame thicknesses δ_L were calculated using the same formula employed in [31]: $\delta_L = 2.3\alpha/S_L$, where α is the mean thermal diffusivity.

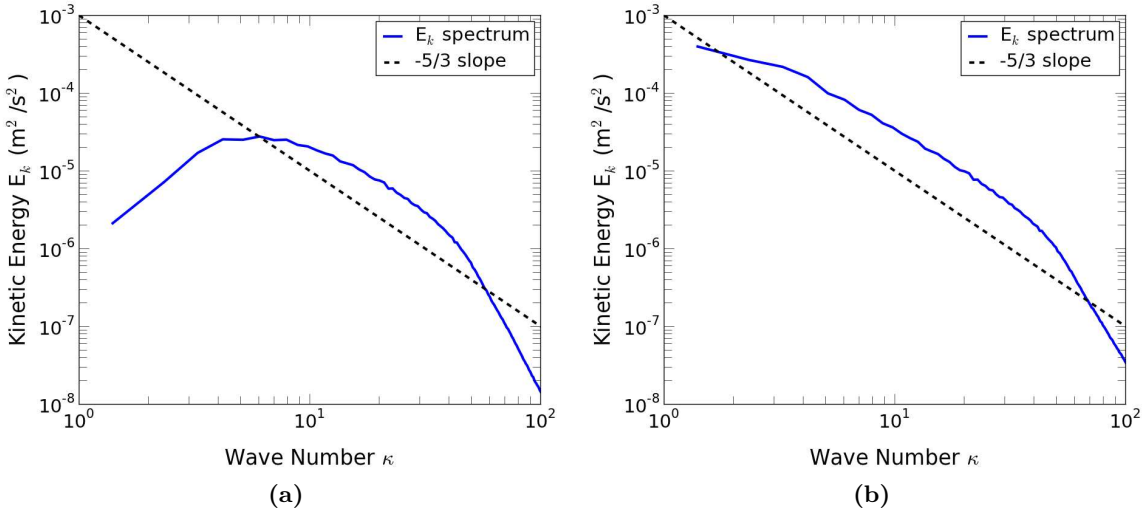

Fig. 15: Kinetic energy spectra for (a) $u' = 0.18$m/s and (b) $u' = 0.34$m/s cases.

As mentioned previously, most previous computational studies turbulent spherical flames initialized their simulations using a laminar spherical flame solution which was super-imposed on the isotropic turbulence [41, 15, 14, 37]. Again, the justification was that in the full-ignition problem, the flame propagates in a laminar fashion for a period of time before the turbulence begins to interact with the flame front. A similar methodology was employed in the current

study. However, obtaining a true spherical laminar flame solution would require reformulation of the governing equations in polar coordinates, or using the existing formulation and solving the equations on a spherical grid. One could develop a spherical laminar flame on a Cartesian grid by initializing a smaller thermal "spot" and allowing it to develop into a laminar flame until the target flame size is acquired. Yet, this would require very high resolution in order to preserve the spherical flame shape during growth from a relatively small to larger radius.

In the current study, the laminar spherical flame was initialized using the solution for a quasi-spherical 1-D laminar flame. This approximation can be justified using the analytical solution for an infinitely thin convex spherical flame:

$$u_A(r) = \left(\frac{R_A(t)}{r}\right)^2 \left(1 - \frac{\rho_b}{\rho_A}\right) \frac{d}{dt} R_A(t) \tag{24}$$

where the subscript A is used to denote the convex flame, $R_A(t)$ the radius of the flame at time t and $u_A(r)$ is the radial velocity at a radial distance of r. Comparing this to the equation for the concave flame:

$$u_B(r) = \left(\frac{R_B(t)}{r}\right)^2 \left(1 - \frac{\rho_u}{\rho_B}\right) \frac{d}{dt} R_B(t) \tag{25}$$

where the subscript B denotes the concave flame. Assuming differences in stretch effects are negligible, it can be assumed that for a convex and concave flame of the same radius R, both flames propagate at the same speed $\frac{d}{dt}R$ but in different directions.

$$\frac{d}{dt} R_A(t) = -\frac{d}{dt} R_B(t) \tag{26}$$

We can use this relation and equations 24 and 25 to relate the flow velocities of both flames.

$$\frac{u_A}{u_B} = -\frac{\left(1 - \frac{\rho_b}{\rho_A}\right)}{\left(1 - \frac{\rho_u}{\rho_B}\right)} \tag{27}$$

Knowing that the velocity inside of the sphere must be equal to zero in the stable solution

$(u_A(r < R) = 0; u_B(r < R) = 0)$, we are interested in the the velocities for $r > R$. Here, $\rho_A = \rho_u$ and $\rho_B = \rho_b$. Replacing these equalities into eq. 27, we see that the mass flux in both cases are equal:

$$\rho_u u_A = \rho_b u_B \tag{28}$$

Therefore, the relation between the velocities is proportional to the ratio of the densities, $u_A = \frac{\rho_b}{\rho_u} u_B$. We can go further to approximate the velocity of the concave flame using that of the 1-D laminar planar flame, where the analytical solutions are related by the square of the normalized radius:

$$u_B = \left(\frac{R_B(t)}{r} \right)^2 u_p \tag{29}$$

where u_p is the planar flow velocity. In combination with eq. 28, this leads to the following relation for the convex flow velocity:

$$u_A = \left(\frac{R_B(t)}{r} \frac{\rho_b}{\rho_u} \right)^2 u_p \tag{30}$$

The radial velocity profile for the convex flame is then approximated by eq. 30 and the planar 1-D profile for u_p, which is calculated using detailed chemistry. The radial profiles for temperature and species are then approximated directly by those of the planar 1-D solution shown previously. The resulting temperature and velocity radial profiles are shown in Fig.16. The spherical laminar flame is then created through integration of the 1-D radial profiles. The starting simulation solutions for both cases can be seen Fig.17b.

4.1.5 Data Processing

In order to compare the results of the simulations directly to those produced by previous studies, the data were processed in similar fashion as described in Wang et. al. [41]. In order to match the FSD-LES study, the temperature field was converted into a progress-variable form;

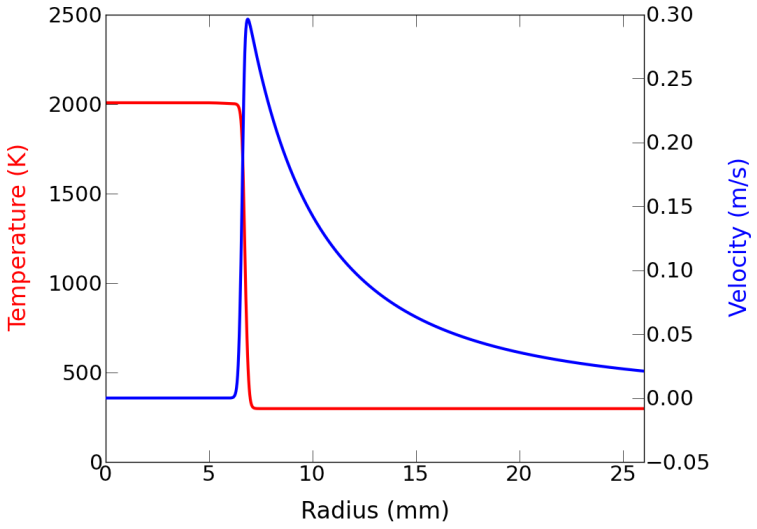

Fig. 16: Radial velocity and temperature profiles used in the spherical flame initialization.

$$c = \frac{T - T_u}{T_b - T_u} \tag{31}$$

where c is the progress variable, T_u and T_b is the temperature of the unburned and burned gas, respectively. This can then be used to calculate the resolved flame surface area:

$$S_{res}(t) = \int_V |\nabla c| dv \tag{32}$$

where V indicates integration over the whole computational volume. The total volume of burnt gases can be estimated as:

$$V_b(t) = \int_V c dv \tag{33}$$

The total flame radius R_p is then defined as the radius of the spherical flame having a total surface area of S_{res}:

$$R_p(t) = \left(\frac{S_{res}(t)}{4\pi} \right)^{1/2} \tag{34}$$

The mean flame radius R_s is defined as that of the spherical flame having the same total

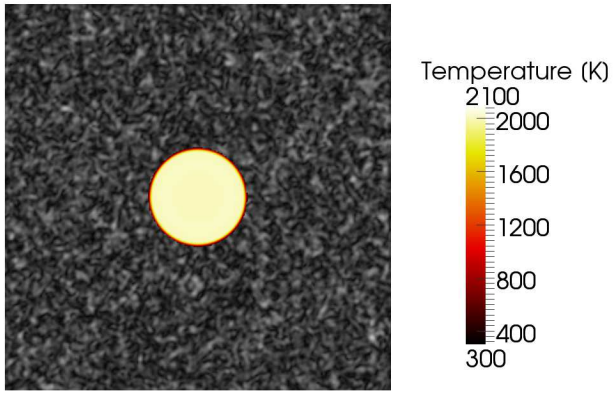

(a)

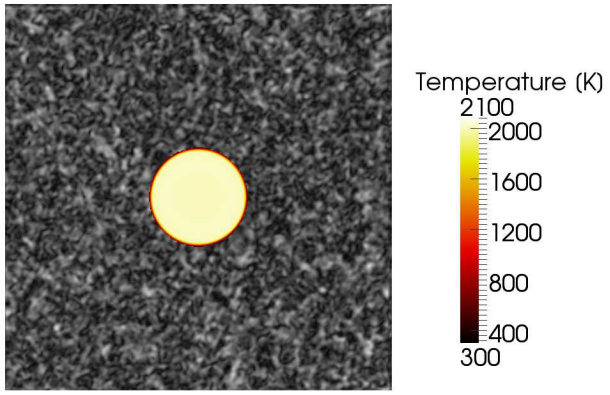

(b)

Fig. 17: Center-plane cut of initial solution for (a) $u' = 0.18$m/s and (b) $u' = 0.34$m/s cases.

volume of burned gas:

$$R_s(t) = \left(\frac{3V_b(t)}{4\pi}\right)^{1/3} \tag{35}$$

4.2 Spark Ignition in a Channel

It is of interest to study the details of spark ignition in a more practical, laboratory-scale configuration, and compare the resulting ignited flame to that of the turbulent spherical problem, which is much more fundamental in nature. The chosen igniter geometry was of the opposing-electrode type, which is the de-facto standard in ignition studies due to it's relatively simple

design and feasibility in the experimental setup. This will also allow for comparison of to many previous studies, both numerical and experimental, that have used a similar configuration . Additionally, an experimental endeavor conducted by Kim and Sforzo was carried out in parallel with the present study, and the overall configuration of the igniter geometry, as well as the operating conditions, were chosen to match that being used by their experiment.

Many applications of spark ignition systems contain a mean bulk flow velocity (such as those found in rocket or turbine engines). This will doubtlessly introduce an initial asymmetry compared to the spherical case, since flow interaction with the surrounding geometry (such as the electrodes) will introduce varying degrees of strain which may affect flame development. In this regard, the simulation will be performed in a channel with uniform mean flow velocity, where the electrodes are placed in the cross-stream direction. The effects of practical levels of turbulence with combustion occurring near the TRZ regime will be studied by comparing cases having either laminar or turbulent inflows. A fuel-lean CH_4/air mixture of equivalence ratio $\Phi = 0.6$ was used, as done in the experiment.

Since ionized fuel chemistry was not available in the literature (at the time of the study), positively-charged species and electrons were not included in the combustion studies. Instead, since it is widely thought that ionization affects ignition mainly through the additional production of key radical species by electron-impact decomposition [36, 38], these effects were studied indirectly by modifying spark composition. Specifically, the development of a spark kernel with finite monatomic oxygen concentration at $t = 0$s was compared to that of a kernel with non-decomposed reactants and no radicals initially present. This particular portion of the study was conducted using the laminar inflow condition.

4.2.1 Numerical Solver

In order to appropriately capture the initial shock produced by the spark, an Hybrid differencing formulation was used for the initial $10\mu s$, which incorporated a second-order MacCormack central-differencing scheme and a MUSCL method for resolving local discontinuities. For

times greater than $10\mu s$, only the second-order MacCormack scheme was used in solving for the relevant fluxes. A laminar flame approximation was used where the subgrid flame structure is assumed to be of the laminar type. The unresolved turbulent terms, such as Reynolds stresses, species and energy turbulent fluxes are closed using the LDKM model as described earlier. As before, a thermally-perfect ideal gas assumption is used with mixture-averaged transport. The effect of magnetic fields and radiation was assumed to be negligible.

4.2.2 Computational Grid

The multi-block grid geometry and mesh were constructed using the ANSYS ICEMCFD software package. Most dimensions followed those used in the experimental setup . The length of the channel was chosen such that an adequate distance was used to allow flow development upstream of the electrodes, as well as having a sufficiently long domain downstream of the electrodes in order to capture flame kernel evolution. The grid geometry can be seen in Fig. 18, where many of the relevant dimensions are labeled. Both electrodes were equal in length, had a diameter of 3.175mm and a gap size of 6.35mm. A structured mesh was used, where a cylindrical O-grid was created between the electrode tips and which expanded the a cartesian mesh that spanned the rest of the domain. Various plane global perspectives of the grid can be seen in Fig. 19, with closer views of the O-grid shown in Fig. 20. Between the electrodes, it was necessary to align the cells in the radial direction of early spark evasion in order to preserve the cylindrical shape during this process. Otherwise, the spark cylinder would need to be approximated on a Cartesian mesh, which would cause a distinct "blockiness" on the spark surface and be accentuated during the rapid growth that ensued. The smallest resolution in the O-grid was $\sim 15\mu m$, which was necessary to allow for numerical convergence when solving for the stark gradients produced by the spark initialization (which will be explained shortly). To allow for the flame front to be adequately resolved, the resolution downstream of the electrodes was set to 0.10mm, which is approximately one-eighth of the laminar flame thickness of $\delta_L|_{\Phi=0.6} \approx 0.78$mm.

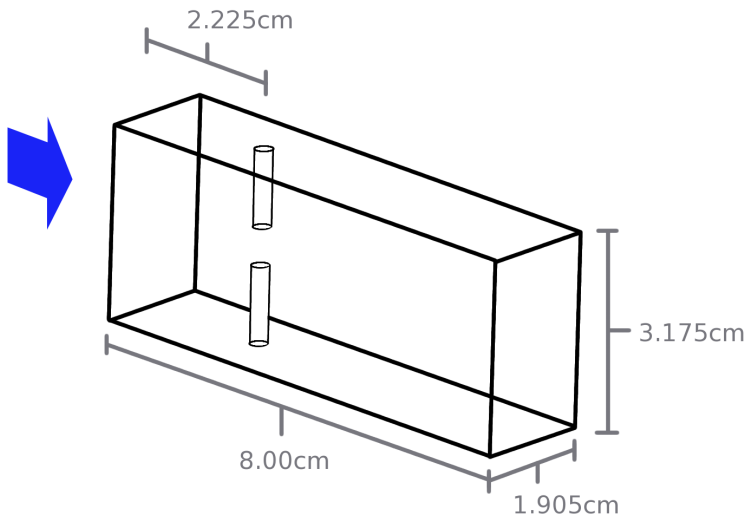

Fig. 18: Channel geometry with cylindrical electrodes. The arrow indicates the inflow location and direction.

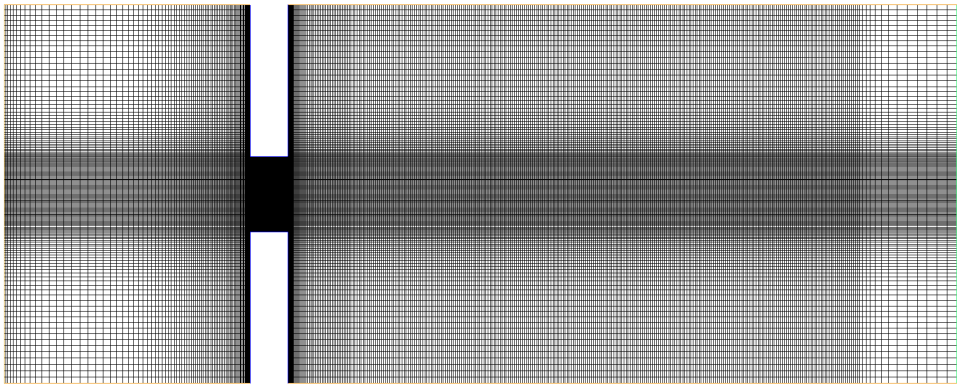

(a) side

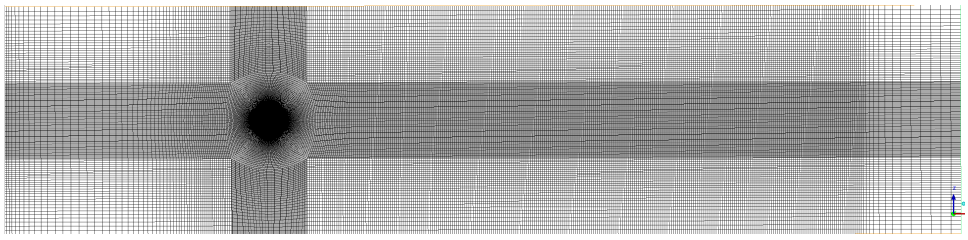

(b) top

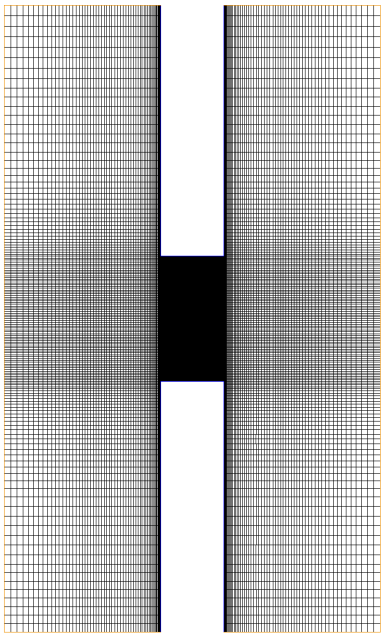

(c) front

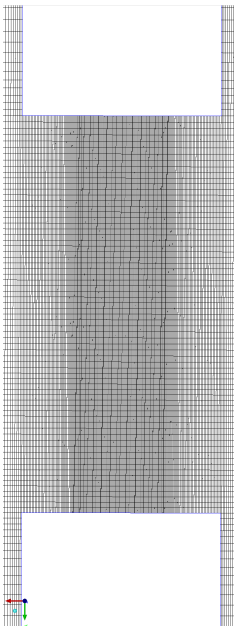

(d) side (zoom)

Fig. 19: Grid structure used in the simulation. Shown are different planar cuts taken through the different axes, where the origin is located at the center point between the electrode tips.

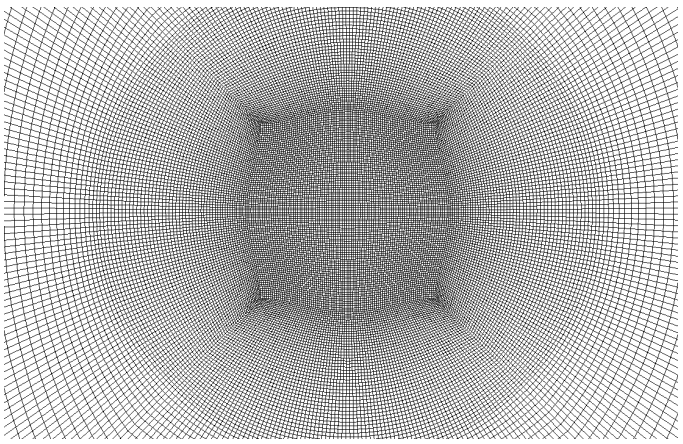

Fig. 20: Close-up perspective of the O-grid structure between the electrodes.

4.2.3 Boundary Conditions

The mean inflow velocity was set to $U_0 = 22.0$m/s to match the experimental conditions. The inlet was given a subsonic non-reflective boundary conditions, in order to allow upstream pressure waves (especially those generated by the spark) to leave the domain. A numerical dampening, or "sponge-averaging" zone, was placed just prior to the outflow in order to dissipate any oscillations propagating downstream without affecting upstream conditions. The outflow boundary condition was therefore set to a supersonic Neumann outflow type (although the flow velocity was consistently subsonic) such that remaining pressure waves were forced to leave the domain. It must be noted that all simulations were performed such that the flame and resulting features were analyzed within the domain of interest and away from the dissipative outflow region (which had a thickness of 2.0mm). All walls were given a no-slip boundary condition.

For the turbulent inflow case, a turbulent rms velocity field was computed using the formulation of Kraichnan et. al. [23] and superimposed on the mean U_0 bulk flow velocity. The velocities were weighted by a power-six profile, which satisfied the no-slip condition for streamwise components, and prevented any finite cross-stream velocities from being attributed at the walls upon injection.

4.2.4 Initial Conditions

Before initializing the spark, the cold flow was developed in the channel for both laminar and turbulent inflow cases. This was performed at a temperature and pressure of 300K and 1 atm, respectively. The cold flow was simulated over 2-3 flow-through times in order to allow pressure waves from the initialization to leave the domain and for flow features, such as boundary layers and vortex shedding, to become statistically stable. The velocity and vorticity distributions in the laminar flow can be seen in Fig. **??**, whereas the turbulent case is shown in Fig. 21. It is apparent in both cases that a significant recirculation zone has developed downstream of the electrodes, with a wake that extends to the end of the channel domain.

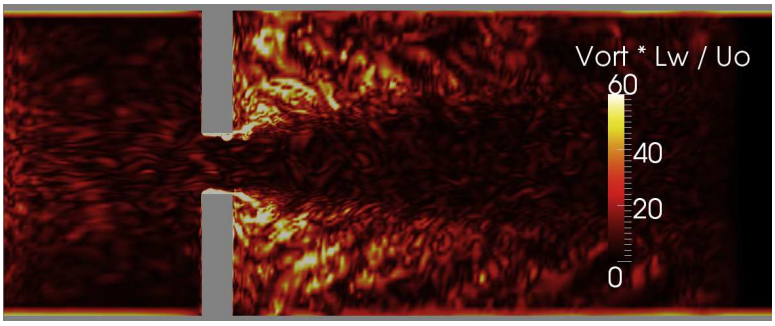

(a)

Fig. 21:

Statistics were gathered for the turbulent inflow case in order to ensure that the turbulence had become statistically stable. The rms velocity distribution is shown in Fig. 24, and it appears to be fairly uniform upstream of the the electrodes, as well as between the electrodes and the wakes. The profile of the rms velocities along a the streamwise center-line (Fig. 23) shows that the turbulence upstream of the electrode leading edge is essentially isotropic. An rms velocity of 1.0 m/s is obtained just before the electrodes, which amounts to an intensity of 4.5% and matches that measured in experiment. Although the centerline passes between the electrodes, the presence of the protruding geometry can be felt midstream. This can be seen by the increase in the streamwise component of the rms velocity.

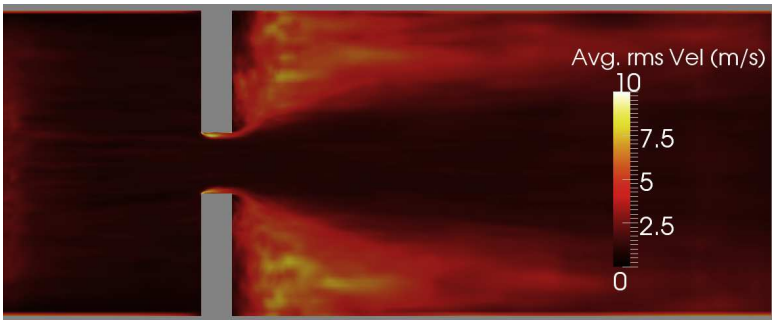

Fig. 22: Cut-plane in the cross-stream direction showing the distribution of the rms velocity magnitude.

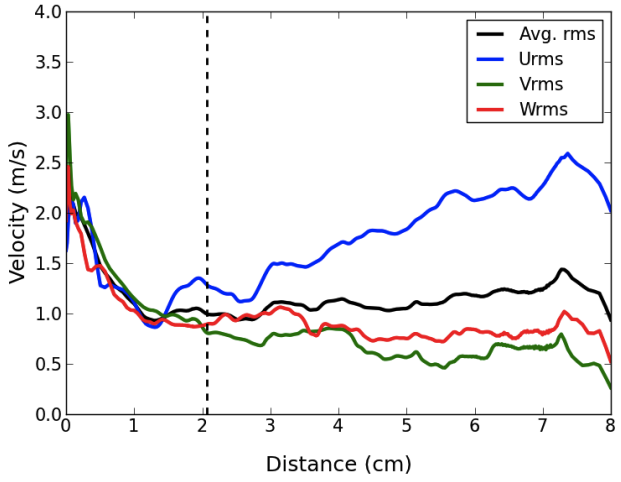

Fig. 23: Distribution of average rms velocities and three-dimensional components. The dashed line indicates the location of the electrode leading edge.

The time-integrated energy from spark deposition in the experimental setup was calculated to be 0.25J, which accounted for heat loses [**?**]. The spark deposition time of the experimental igniter configuration amounted to $0.5\mu s$, which is relatively small compared many previous spark ignition studies which employed spark durations closer to $\Delta t_{spark} \sim 100\mu$s [5, 2] and in which spark energy continued well into flame kernel formation. The characteristic time of the convective velocity produced by the initial expansion τ_{mech} can be approximated as

$$\tau_{mech} \approx \frac{R_{elec}}{c|_{T=300K}} = 4.7\mu s \tag{36}$$

where R_{elec} is the radius of the electrodes, and $c|_{T=300K}$ is the speed of sound at a temper-

ature of 300K. Therefore, if a shock is generate right after the breakdown process, it will not have traveled much more than $\Delta r(t = t_{spark}) = R_{elec}/10$, or one-tenth the electrode radius. With this in mind, the flow was treated as being frozen during spark formation. Therefore, instead of modelling the time-varying energy deposition, the energy was deposited instantaneously at $t = 0$s. Since typical relaxation timescales of the energy modes is O(η s), the initial spark kernel was assumed to be at thermal-equilibrium. The thermal heating was assumed to take place in a cylindrical volume between the electrode tips. The initial diameter of the cylindrical kernel was set to 2.50mm (compared to an electrode diameter of 3.175mm). This value was chosen as the minimum radial diameter for which the corresponding energy density produced a temperature value and gradient for which computational convergence could be achieved. The temperature distribution was set to be uniform from one electrode tip to the other and varied as a Gaussian profile in the direction orthogonal to the electrodes (Fig.4.2.4).

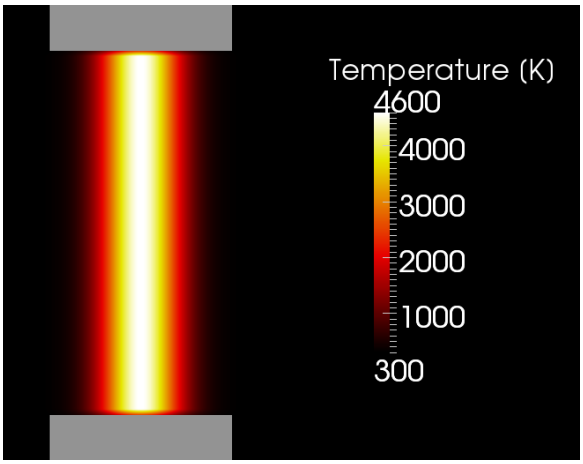

Fig. 24: Temperature distribution of spark initialization.

It is possible that an instantaneous deposition may be an over-estimation, which could result in higher temperatures and pressures than would otherwise be seen in the actual spark discharge (where energy deposition is spread out temporally). In order to justify this assumption, the development of spark kernels in air were first compared to experiment in a preliminary study, which is covered in Appendix A. It was shown that such assumptions

used in the spark initialization produce plasma kernel sizes comparable to those derived from schlieren data in experiment.

Although the spark kernel began at thermal equilibrium, it was assumed that the molecules had not yet begun to react. The initial spark kernel was therefore set to be in chemical non-equilibrium, where the starting composition consisted of unreacted CH_4, O_2 and N_2. It is widely suggested that sparks induce higher early concentrations of key radicals which consequently lead to a faster ignition process. In order to test whether such an effect applied to the present configuration, two nearly different spark initializations were used with the same flow conditions, spark energy and radius. In order to account for early molecular oxygen decomposition and radical pooling, most of the oxygen initially present in one case was in monatomic form. The other initialization did not have any radicals present initially. As the same spark energy was used for both cases, this resulted in different spark temperatures and pressures (owing to the energy used in decomposing the molecular oxygen). The initial spark conditions used in this comparative study are shown in Table 2. The initial temperature and pressure of the spark was determined for a constant volume problem with energy density equal to that found in the initial spark kernel. These values were calculated using the NASA CEA (Chemical Equilibrium with Applications) software .

	Max. Temperature (K)	Max. Pressure (bar)	X_{CH_4}	X_{O_2}	X_O	X_{N_2}
Thermal heating	6317.0	21.9	0.743	0.198	0.059	—
Thermal heating + radical addition	4609.1	18.1	0.656	0.058	0.052	0.234

Table 2: Initial spark kernel conditions (i.e. temperature, pressure and mole fractions) for two different energy distributions: (1) thermal heating only and (2) thermal heating with radical addition.

4.2.5 Chemistry

The chemistry selected for the simulation was a reduced CH_4/air mechanism containing 13 species and 73 reactions [33]. This choice was mainly due to the proven accuracy and minimal temporal stiffness of the mechanism, as well as the inclusion of radical species important to

the ignition processes, such as O, H and OH. The mechanism also includes high-temperature pathways, such as CH_4 decomposition into CH_3. The 1D laminar flame comparison between this chemical mechanism and GRImech3.0 for the chosen equivalence ratio ($\Phi = 0.6$) are shown in Fig. 25, where it is apparent that the species concentrations are fairly well calculated in the chosen chemistry

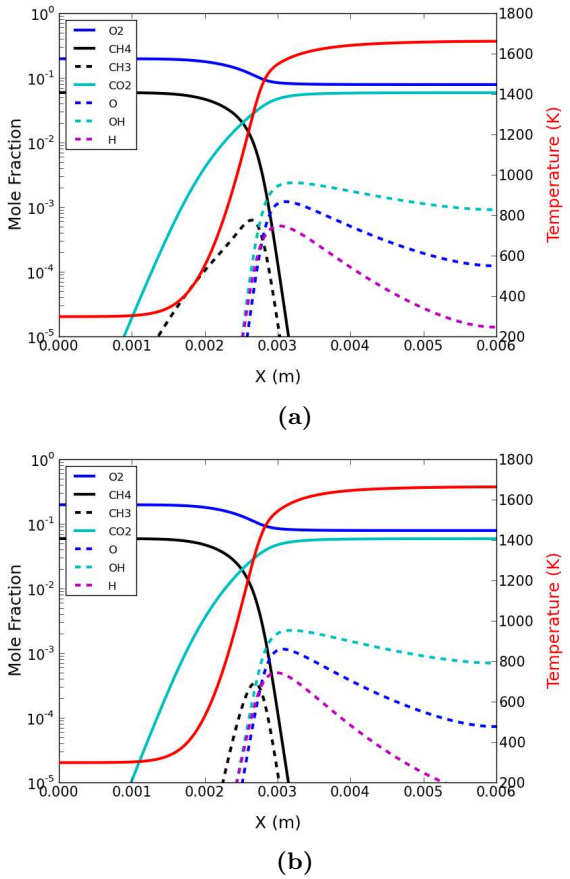

Fig. 25: Species and temperature profiles for a 1D CH_4/air flame ($\Phi = 0.6$) using (a) the 13-species/16-step mechanism and (b) GRImech3.0.

4.2.6 Data Processing

Apart from examining the spatial distributions of properties such as heat-release and temperature over time, it will be useful to account for the degree of mixing occuring between the heated spark kernel and the surrounding cold reactants. For this purpose, the turbulent case will be run using a passive scalar, where an inert species will be introduced in the initialization

to mark the cold gas surrounding the cylindrical spark. This marker will not affect the behavior of the other species present, nor will it affect the energy balance. It will only succumb to the effects of local molecular and temperature gradients as well as convective forces. The passive scalar will be given the properties of the fuel, namely CH_4, and will therefore have the same mass, diffusion coefficients, etc. However, it must be stressed that the marker will not be representative of the actual concentration of methane at any given point in time. It will only be used to track the general convective and diffusive effects occuring in the kernel throughout the simulation.

5 Results

5.1 Spherical Turbulent Flame

The spherical kernels were allowed to develop over 7ms before the edges of the flame came into contact with the domain boundaries. The general effects of heat release and temperature increase were observed in the simulation, namely the rapid damping of vorticity within the flame due to increase in viscosity, as well as changes in the strength of vortices aligned with the flame front. Upon comparison to the results from Wang et. al., the overall flame sizes sizes appeared to be fairly similar over time. Although a detailed chemistry was used, in order to allow for comparison with the previous FSD-LES results a progress variable c was calculated post-simulation:

$$c = \frac{T - T_u}{T_b - T_u} \tag{37}$$

where T_u and T_b is the nominal temperature of the unburned and burned gas, respectively. The flame surface was approximated as being defined by $c = 0.5$, as was done in Wang et. al. . The iso-surfaces for selected times were compared to the independent results and shown in Fig. 26 for Case B ($u' = 0.18$m/s) and Fig. 27 for Case C ($u' = 0.34$m/s). Qualitatively, it is apparent that for Case B, the sizes of the flame appear to be relatively similar between both studies. However, the degree of flame wrinkling is seen to be moderately different between the two flames. The scales of the wrinkling for the current study appear to be, on average,

larger in scale than those in the case of Wang et. al., which seem to be more corrugative and equally distributed. In Case C, the differences in the result are more evident. The flame surface in the reference study appears to be heavly wrinkled by the large turbulent motions with a a more closely uniform distribution. The flame in the current study is not as heavily wrinkled, but is actually distorted on a global level which causes it to deviate from a spherical average flame shape. This can be seen to begin early on, near 1ms, as even at this time there is a large "dent" occuring on one side of the flame, which is exacerbated over time as the flame grows.

The cross-sections of solutions for both Case B and Case C at $t = 6$ms are shown in Fig. 28. Clearly, the turbulence in the unburned gas is seen to contain much larger scales in the $u' = 0.34$ case compared to $u' = 0.18$. Additionally, the vorticity is apparently stronger in Case C. Most importantly, however, it is seen that the turbulent structures seem much less isotropic in the case of more intense turbulence.

The comparison in the R_s and R_p distributions over time between the present results and those of FSD-LES and experiment are shown in Fig. 29. Flame wrinkling typically tends to increase the surface area of the flame front, whereas the volume of the flame for a given point in time is not drastically altered. However, the effect on flame volume is indirect, as turbulence enhances the consumption speed, which increases volumetric growth rates. With this in mind, it is apparent that the radial range of the two plots is different; as total radius R_p values are more affected by flame surface wrinkling, these values tend to be slightly higher than those for R_s, the mean radius.

It is apparent that the resulting radii for Case C appear to agree fairly well with those of Wang et. al., despite the observed qualitative differences in the surface wrinkling. This indicates that although the mean radius of curvature may be different, the net effect on the turbulent flame speed of the stoichiometric propane flame is effectively the same for such turbulence levels. In other words, the increase in flame surface area is the same whether you

have many smaller wrinkles or fewer larger ones, as long as the distributions are uniform throughout the flame fronts. The radial values for Case B in the reference cases begin the deviate from those of Case C after 1-3ms, at which point the surface of the flame becomes much larger due to increased degrees of wrinkling.

The values of Case B from the present study, on the other hand, seem to lie on top of those for Case C. This is most likely due to the fact that although the flame is distorted due to large turbulent scales, this has little impact on the surface area. The degree of wrinkling due to smaller scales, however, is similar to those of Case C. The resulting increase in surface area is then almost the same. The difference in Case B between the present and reference result is due to the difference in turbulent lengthscales. Although the initial nominal values were found to be almost the same (as shown in Table 1), the distribution of the length scales and the turbulent kinetic energy are probably quite different. The amount of energy in the largest scales for the present study are much greater, contributing to the observed anisotropic average flame growth. However, for the reference cases, there is more energy concentrated in smaller scales, which contributed to the large degrees of wrinkling seen to cause increased flame growth. Additionally, although the turbulent structures should not be greatly affected by the boundaries for distances that are one integral length scale from the domain limits, large eddies deviating from the statistical mean might be felt even further into the domain.

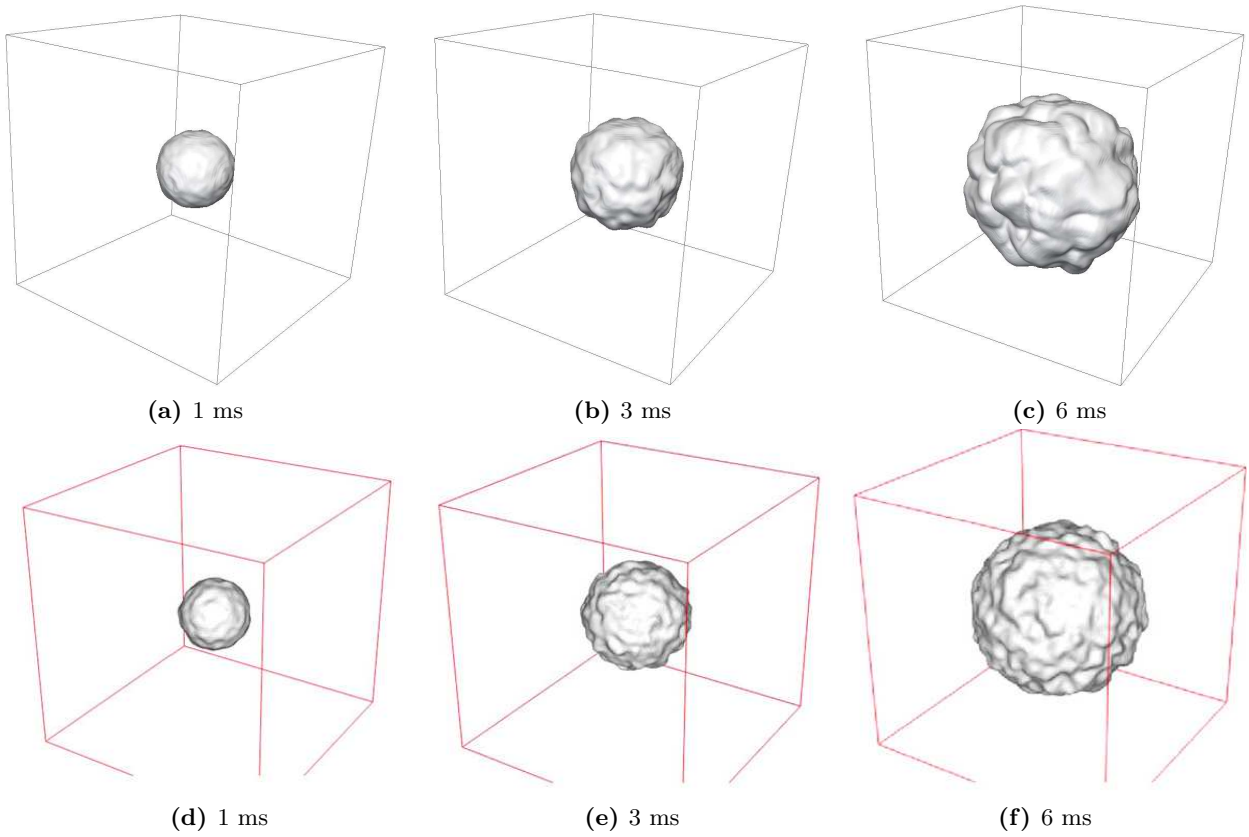

(a) 1 ms **(b)** 3 ms **(c)** 6 ms

(d) 1 ms **(e)** 3 ms **(f)** 6 ms

Fig. 26: Iso-surfaces for $c = 0.5$ for Case B ($u' = 0.18$) comparing results from the present study in (a), (b),(c) to those from Wang et. al. in (d), (e), (f).

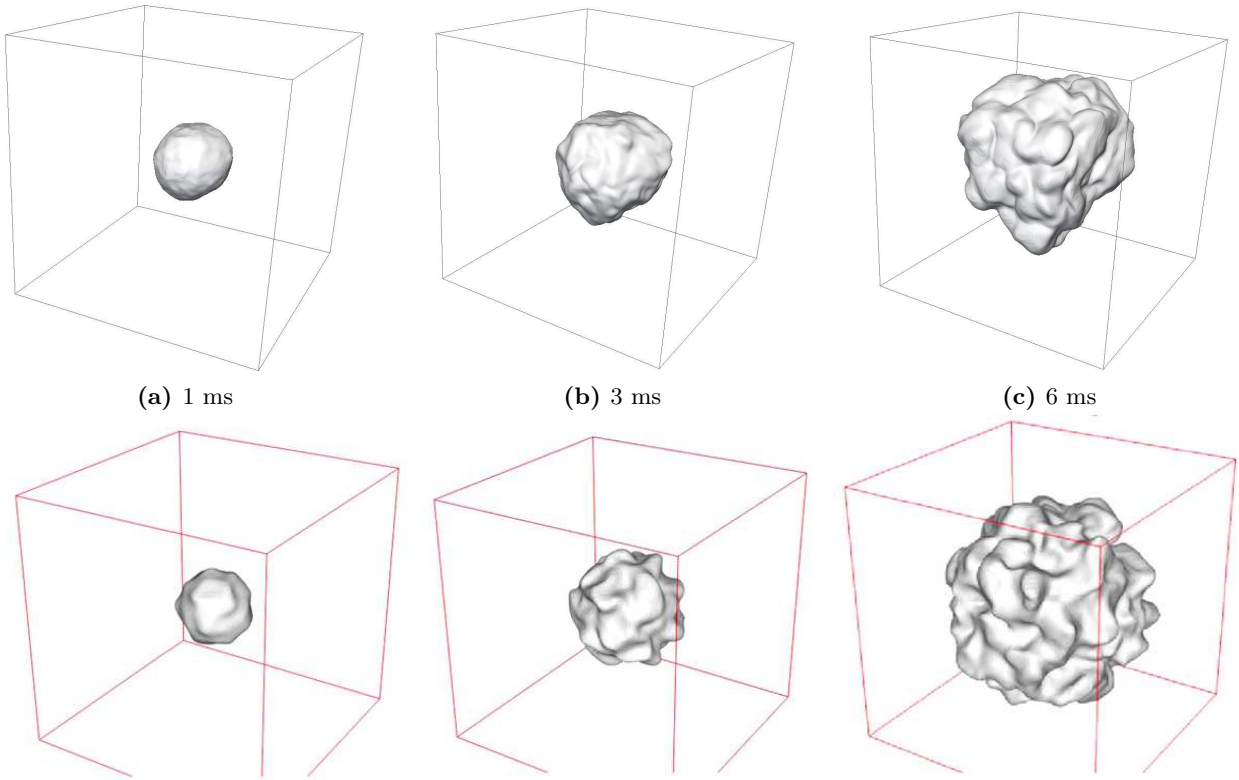

(a) 1 ms **(b)** 3 ms **(c)** 6 ms

(d) 1 ms **(e)** 3 ms **(f)** 6 ms

Fig. 27: Iso-surfaces for $c = 0.5$ for Case C ($u' = 0.34$) comparing results from the present study in (a), (b),(c) to those from Wang et. al. in (d), (e), (f).

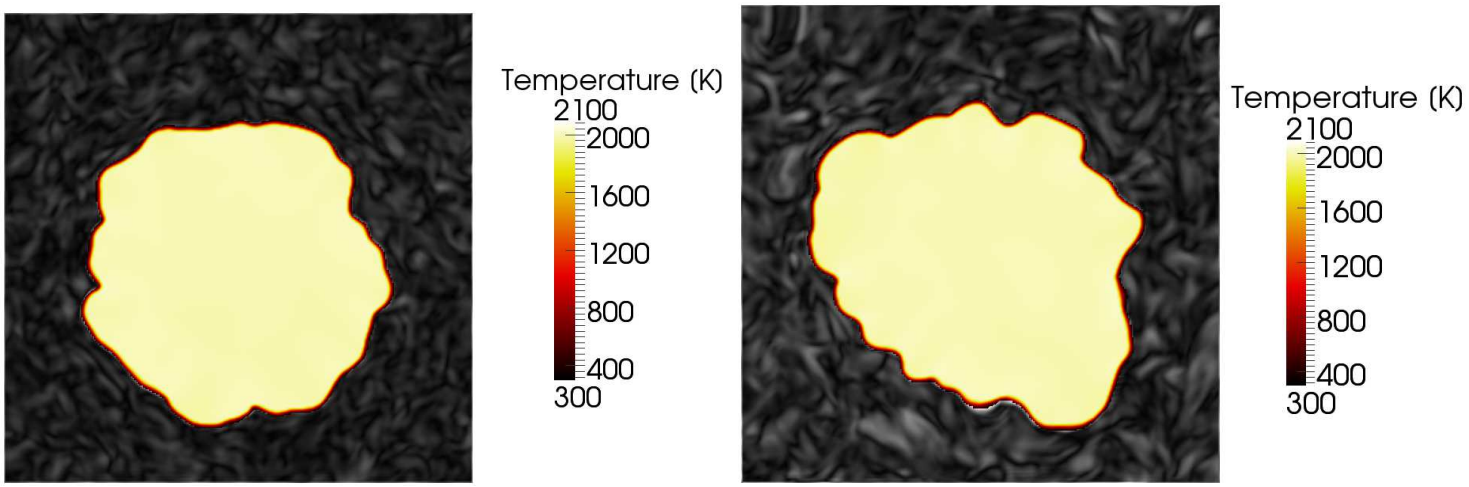

(a) **(b)**

Fig. 28: Center-plane distributions of temperature (for $T > 600$) superimposed on vorticity for (a) $u' = 0.18$ and (b) $u' = 0.34$

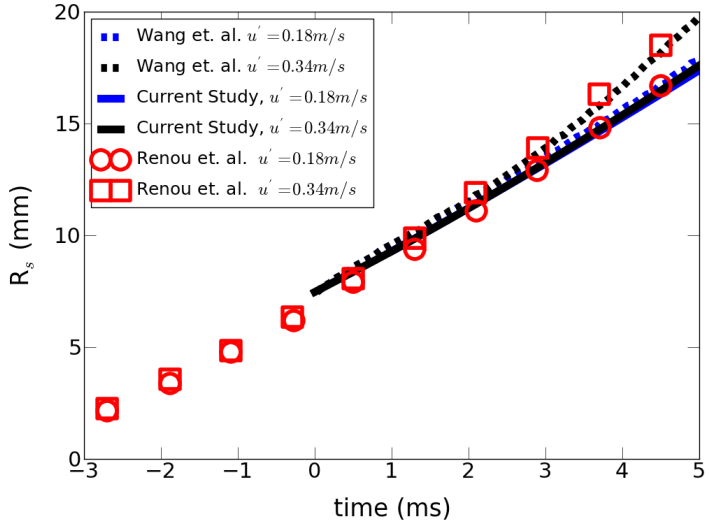

(a)

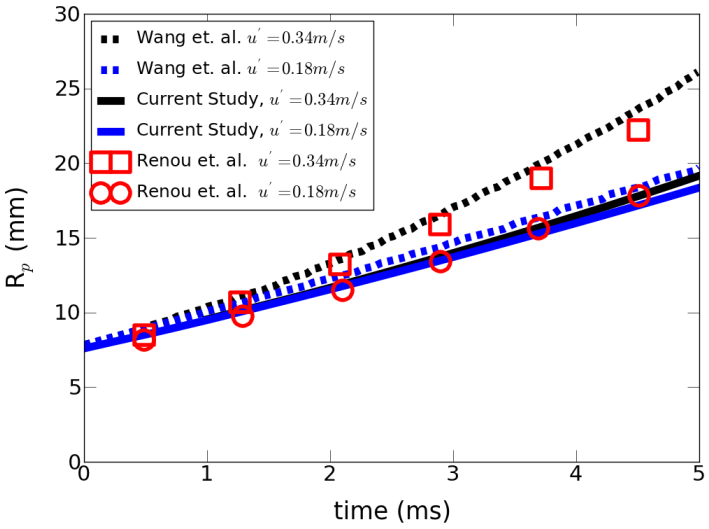

(b)

Fig. 29: Mean radius R_s and total radius R_p with time (where $t = 0$ is the start of the simulations) for both Case B and C comparing the results of the present study to those from FSD-LES (Wang et. al) and experiment (Renou et. al.).

5.2 Spark Ignition in a Channel

At the moment of sparking the electrodes, the high pressure and temperatures in the cylindrical volume cause the gas to expand rapidly towards the edges of the electrode. This early expansion phase appeared to last as little as 1μs, during which it was apparent that the peak temperature in kernel had dropped by $1000 - 2000K$. According to the simulation, the high temperatures cause reactions to occur even at this early stage, where the fuel within the kernel is consumed almost instantaneously. Following this, fuel consumption is seen occuring on the outer edges of the expanding spark kernel, e.g. at the interface between burned and fresh gases.

The high temperature and pressure from spark initialization generates a shockwave which is coupled to the expanding gas in the first $1-2\mu$s, which is similar to what had been observed in the litterature. The decoupling occurs once the expanding spark kernel reached the edges of the electrode. At this point, the shock-induced rare-faction at the edges initiated heavy recirculation around the rims of both electrode edges. This caused the hot gas propagating in the direction of the shock nearest to the rims to be drawn back towards the electrodes, and at the same time entraining unburned reactants into the kernel. Although a bulk velocity was present throughout the channel, the high pressure gradient present during the shock-expansion phase was strong enough to drive the gas expansion in a cylindrically-symmetric fashion. Only after $t \sim 10\mu$s did the kernel begin to become convected by bulk flow velocities and pushed away from the electrodes. During this time, the shock fronts reflect off the walls of the channel and return as rare-faction waves towards the centerline. Due to these acoustic oscillations, the flame kernel undergoes slight compression/expansion during the first $\sim 200\mu$s before the pressure waves have mostly dissipated.

Ther kernel begins to convect downstream from the electrode as the shock-induced entrainement is drawing the unburned gas in towards the central core of the kernel. These two processes act in concert to produce a toroidal-like shape, where the downstream portion is larger in volume than the upstream side. The hole of the toroid is formed when the two

entrainement streams moving from the electrode tips meet in the center, where they proceed to "pinch-off" and separate the sides of the toroid from each other. This occurs between $50-100\mu$s, which is folowed by continued convection of the downstream portion of the toroid. The pinching process causes the entrainment streams to mix with each other and produce a region of high vorticity on the upstream portion of the flame kernel. Along with observable flame-holding occuring at the eletrode edges, these upstream effects result in a lower bulk velocity compared to the downstream portion. The disparity causes the the flame kernel to lengthen in the streamwise direction before size before the recirculating upstream portion also begins to convect away from the electrode geometery.

5.2.1 Thermal and Radical Effects

Although the actual spark break-down and ionization processes were not explicitly modeled in the simulation, the speculated effect of increased radical concentrations due to plasma effects was tested. As mentioned earlier, this was done by comparing flame kernels produced via two different spark initializations. The first simulation was conducted by starting with a cylindrical spark with a raised temperature and pressure. This will be reffered to as the thermal case, as the energy deposition is assumed to increase the thermal energy only. The second simulation began with a cylindrical spark containing the same amount of net energy, but distributed chemically as well as thermally. This is the radical case, as a portion of the energy was used to produce decompose most of the molecular oxygen in the spark volume to produce a quantity of oxygen radicals, which are known to be a key element to the ignition (as well as combustion) process. The majority of the energy is still stored in thermal modes, however, and it must be noted that the name of the case does not imply that no energy is stored thermally.

As is apparent in Fig. 30, there is not an appreciable difference in the resulting shape and size of the flame kernel between the two case at times $t < 10\mu$s. Both appear to go through the same general process of symmetric expansion and shock generation. The strength of the pressure wave also seems to be very similar for both cases. However, the thermal case does

appear to have a moderately higher temperature at the kernel edge, which is unsurprising due to its higher initial temperature. The heat release is also similar, as is shown in Fig. 31 where the heat-release $\dot{Q}$ is normalized by the peak value in a laminar planar flame of the same equivalence ratio. The degree of reaction is noticeably much greater in this case, which is attributable to the large temperatures involved. The reaction front in both cases appears to be fairly uniform between the electrodes. It is noticeable, though, that $\dot{Q}$ is marginally larger in the radical case compared to the thermal. The differences at 2.5μs between both cases are examined more closely in Fig. 32, where the streamwise centerline values through the kernels are plotted against each other. It is clearly seen that all the fuel that began within the hot kernel volume has been consumed. Although the thermal case began without any radical concentration present, at this point in time it has produce almost the same extent of atomic oxygen as in the radical case. In combination with the profiles of hydroxyl radical and carbon dioxide, it is apparent that the internal kernal volume is still far from chemical equilibrium. The fuel consumption and heat-release distributions are also shown in Fig. 32e and Fig. 32f, where negative fuel consumption is normalized by the peak CH_4 in a laminar planar flame. Both cases show that the heat-release is directly correlated to fuel consumption. It does appear, however, that consumption is slightly stronger in the thermal case.

The temperature distributions are shown in Fig. 33, where it can be seen that at 214μs there is still a significant degree of thermal energy left which originated from the spark kernel. The adiabatic flame temperature for $CH_4|_{\Phi=0.6}$ is approximately $1700K$, which means that most of the dowstream kernel is still overheated by residual spark energy. This appears to sustain much of the combustion in this region, as is depicted in Fig. 34. Although high temperatures are present in the upstream portion, there is much less reaction taking place in this region compared to the downstream side. The center-line plots in Fig. 35 show that the inner portion of the downstream kernel contains mostly hot products at this point in time, although there are still significant concentrations of radicals present.

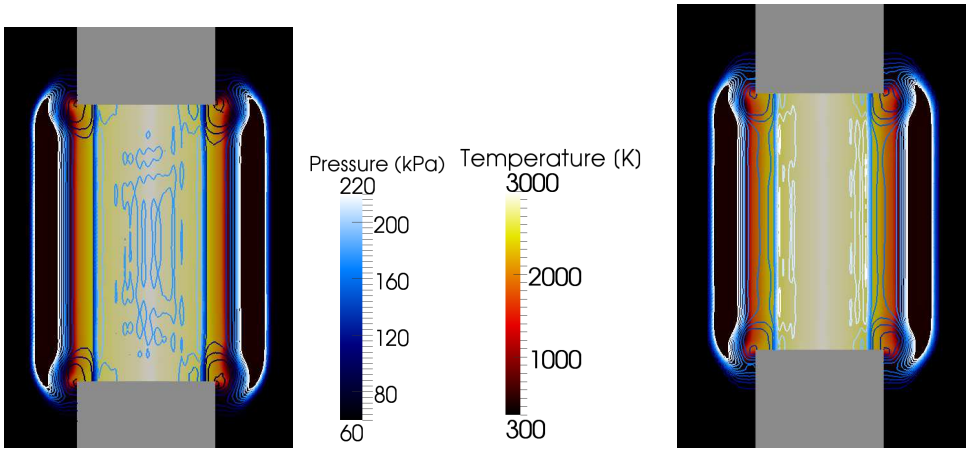

(a) **(d)**

Fig. 30: $t = 2.5\mu$**s:** Temperature distribution with pressure contours in a centered side-cut plane for the (a) thermal and (d) cases.

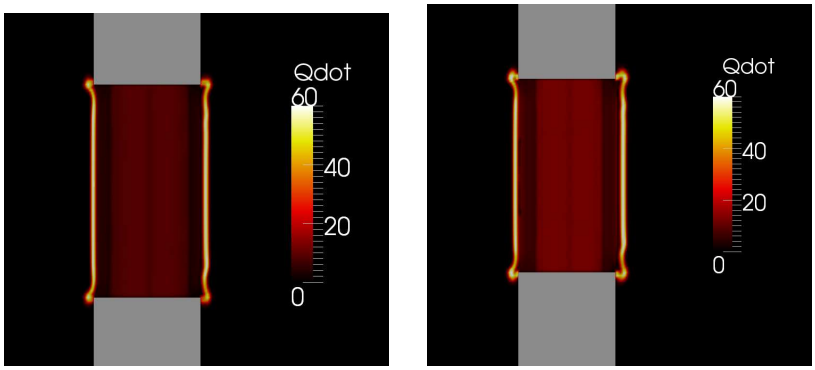

(a) 2.5 μs **(b)** 2.5 μs

Fig. 31: $t = 2.5\mu$**s:** Normalized heat-release distribution per volume in a centered side-cut plane for the (a) thermal and (b) cases.

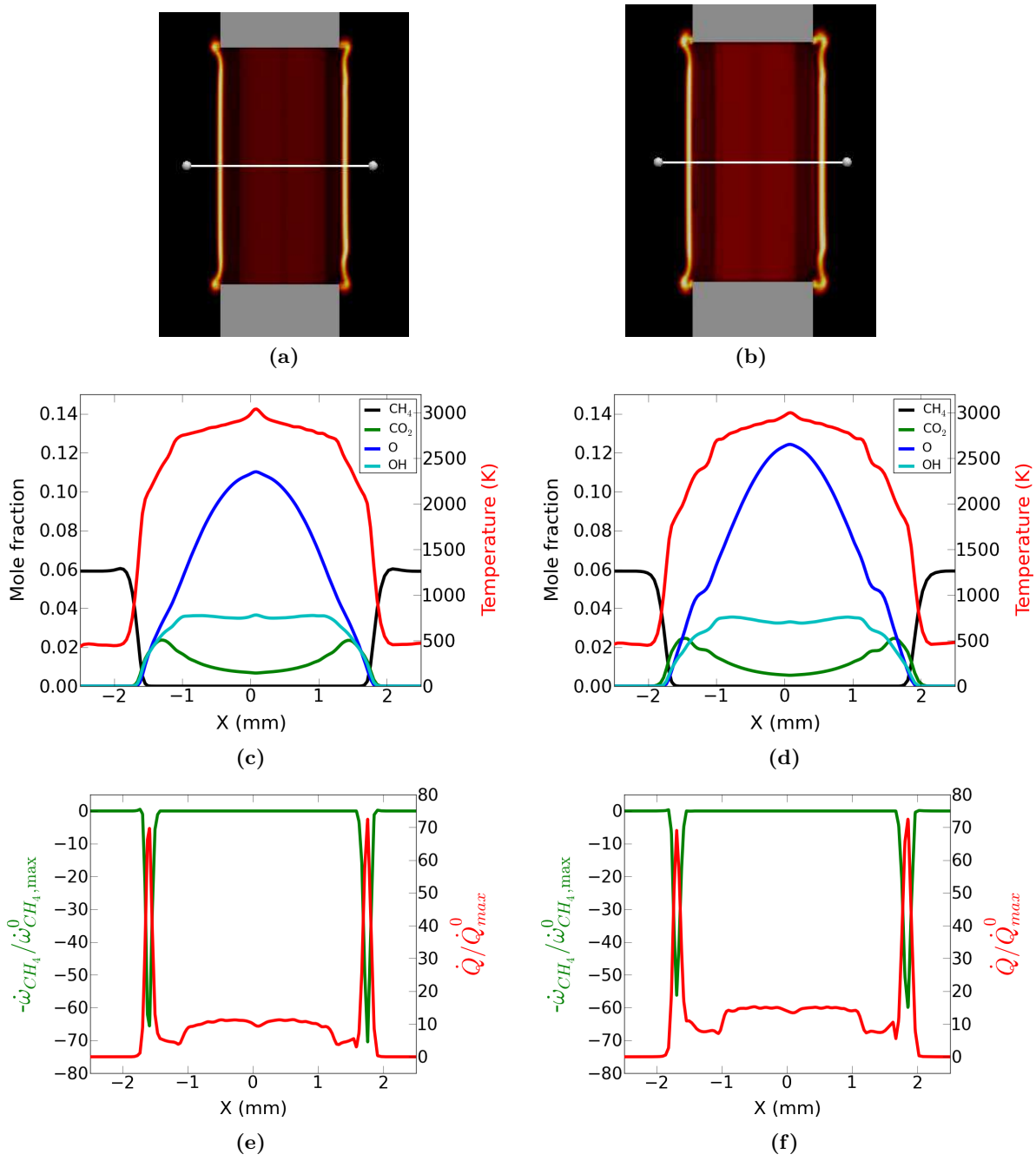

Fig. 32: $t = 2.5\mu$**s:** Center-line plots of temperature, species concentrations, normalized fuel consumption and heat-release for thermal (left) and radical (right) cases.

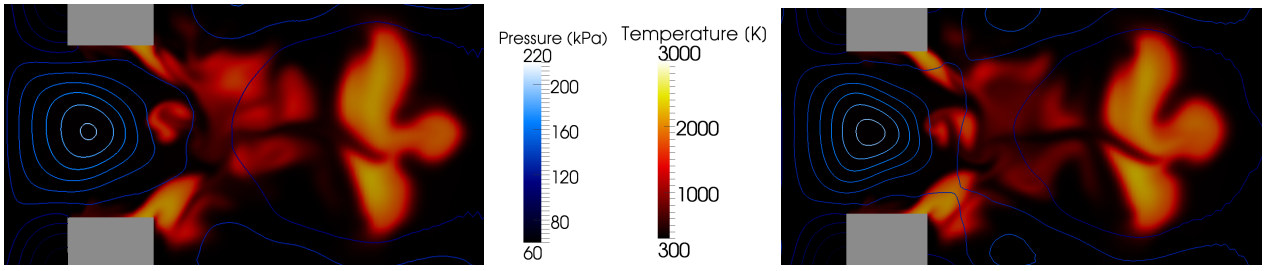

(a) thermal (side-cut)

(d) thermal & radical (side-cut)

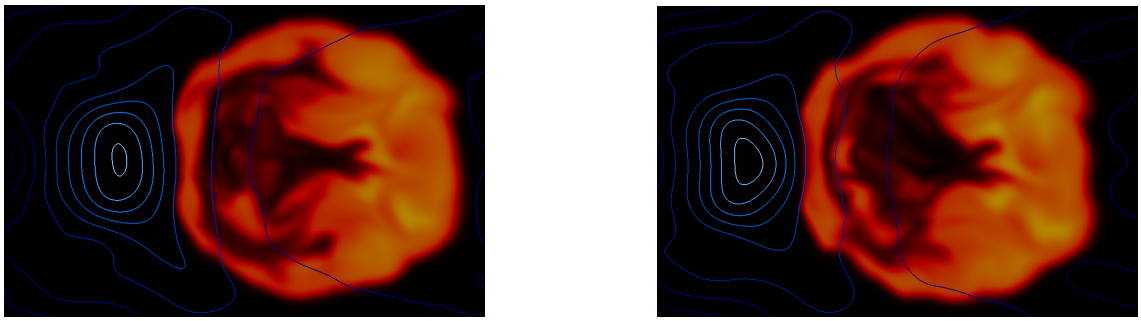

(e) thermal (vertical-cut)

(f) thermal & radical (vertical-cut)

Fig. 33: $t = 214\mu$**s:** Centered side- and vertical-cut planes showing temperature distributions and pressure contours for the thermal (left) and radical (right) case.

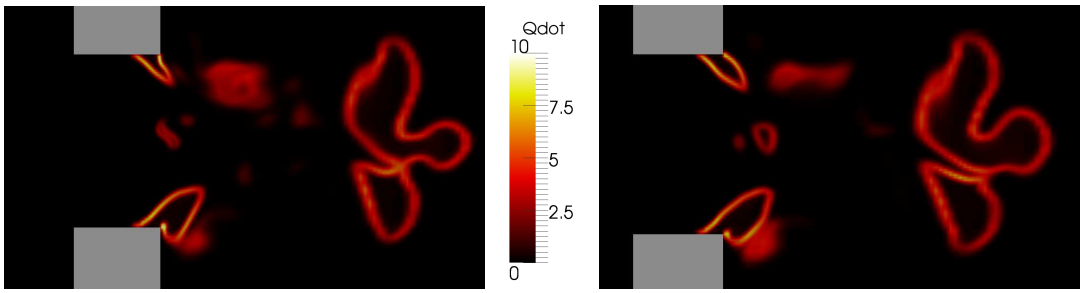

(a) thermal (side-cut)

(c) thermal & radical (side-cut)

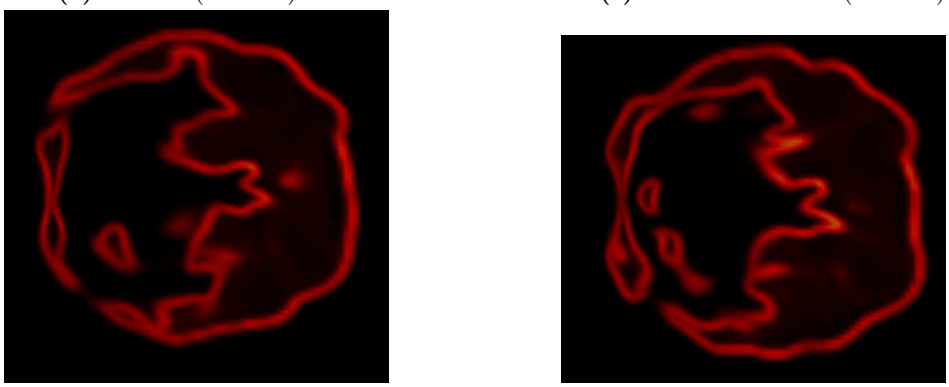

(d) thermal (vertical-cut)

(e) thermal & radical (vertical-cut)

Fig. 34: $t = 214\mu$**s:** Centered side- and vertical-cut planes showing normalized heat-release per volume for the thermal (left) and radical (right) case.

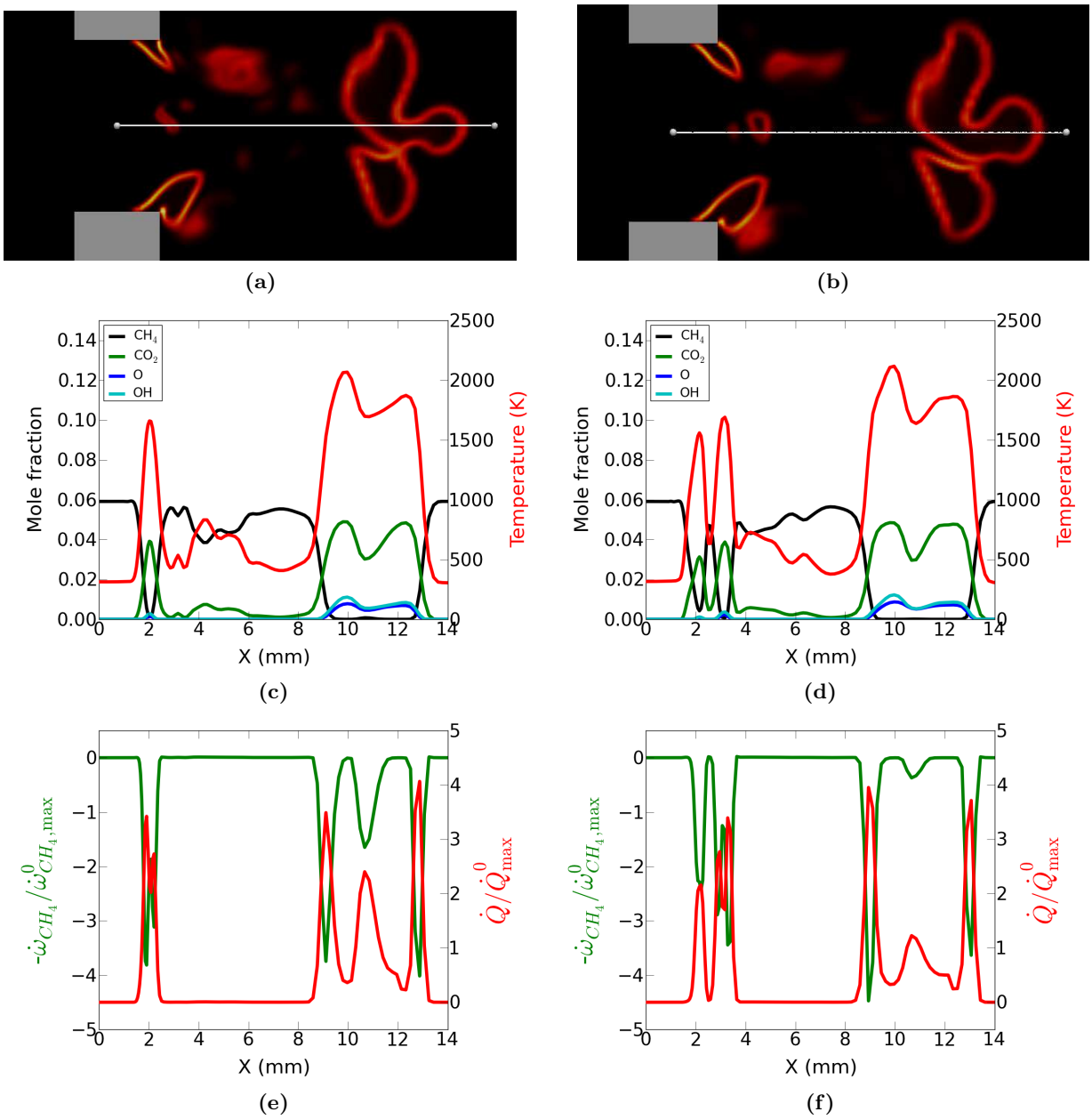

Fig. 35: $t = 214\mu$**s:** Center-line plots of temperature, species concentrations, normalized fuel consumption and heat-release for thermal (left) and radical (right) cases

5.2.2 Laminar vs. Turbulent Inflow

The laminar and turbulent cases both generated flame kernels which evolved into larger propagating flame fronts. The simulations showed similar results for times $t < 10\mu$s. Fig. 36 demonstrates that both cases produced relatively similar temperature distributions. The shockwave generated in either case appears to be of similar magnitude, causing the same degree of recirculation at the electrode edges. Fig. 37 shows that the the levels of reaction in the cases are also similar at this time. Near 50μs, both cases are already well into the entrainement phase, where the leading kernel lobe has begun to form on the downstream portion . Since the time shown for the turbulent inflow case in Fig.38 is slightly ahead of the laminar inflow case by $\sim 3\mu$s, the reflecting pressure waves have progressed further, and can infact be seen to distort the circular shape of the kernel vertical cross-section (Fig.39f). A closer glance offered in Fig. 39 shows noticeably different temperature distributions in either case. The front of the lobe in the laminar inflow case appears to have larger regions of high temperature. Although there is a temporal disparity in this particular comparison, the temperature difference will be addressed further on. The heat-release rates depicted in Fig.40 clearly indicate effect of the entrainment vortice on the flame front; the flame is pulled inwards along with a stream of fresh reactants. The induced concave flame stretch causes an increase in local heat release.

At $t = 100\mu$s, the difference in both cases becomes apparent. The kernel in the laminar inflow case has progressed further out, indicating that the local convective velocity is greater, possibly owing to larger outward push due to stronger entrainement velocities. The strength of the entrainement vortices are in fact shown to be larger in the laminar inflow case (Fig.42), which causes a stronger outward convective velocity in the central plane leading the downstream lobe to fold back further. This portion of the kernel is found to be higher in temperature in the laminar inflow case until much later on. This is seen in Fig. 43, where the downstream half is generally much hotter and larger as well. However, it appears that a greater degree of mixing occurs in the turbulent inflow case, resulting in enhanced combustion on the upstream portion. This is most noticeable upon examining the heat release

distributions in Fig. 44, where it seems that a greater number of burning pockets exist in in the turbulent inflow simulation. It is also worth noting the existence of vorticale structures persisting within the kernel. Furthermore, it can be seen that the kernels contain many vortical structures which persist throughout the simulation. These do, however, begin to dissipate as is seen later on at $t = 800\mu$s (Fig. 46). At this time, the effect of turbulent burning enhancement at the trailing edge is seen most noteably in Fig. 45.

Three-dimensional perspectives of the temperature iso-surface for $T_{iso} = 1700K$ is shown in Fig. 47 and Fig. 48. For the first hundred microseconds, both kernels appear to be very similar in volume. At these times, it is clear that there is no significant degree of wrinkling due to turbulent interaction with the flame front. However, differences in the surface of the flame and corrugation of the flame front are apparent close to 800μs.

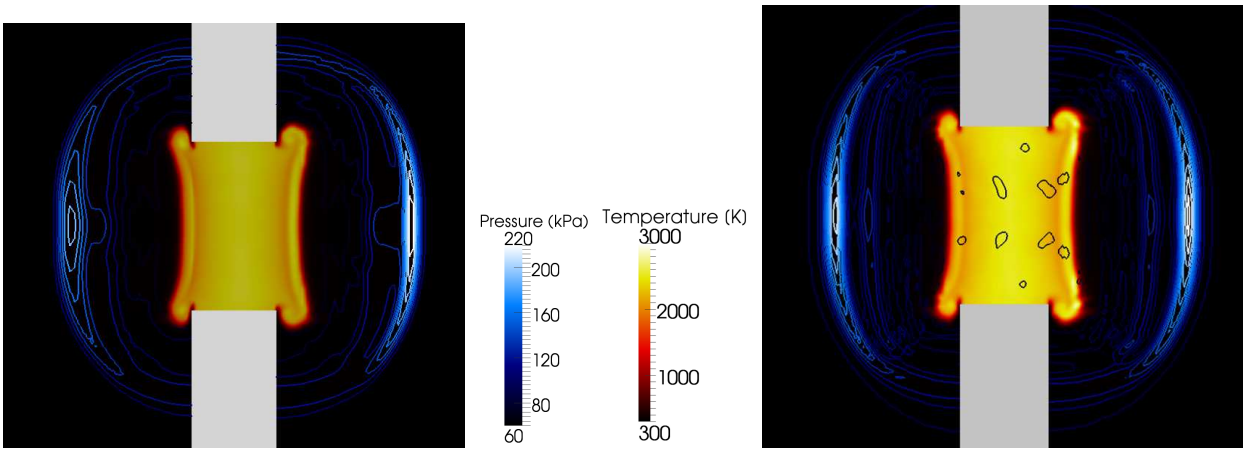

(a) side-cut

(d) side-cut

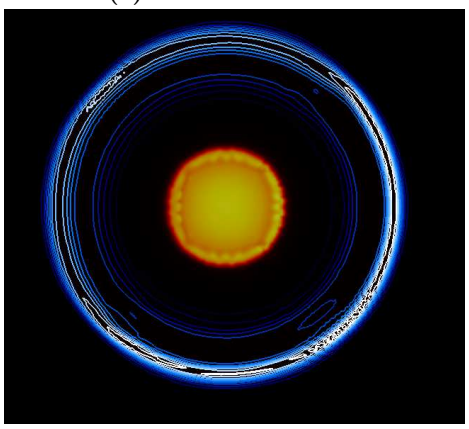

(e) vertical-cut

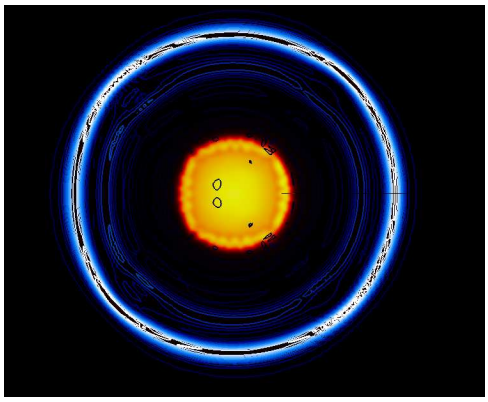

(f) vertical-cut

Fig. 36: $t = 10\mu$**s:** Temperature distribution with pressure contours in centered side-and top-cut planes for the laminar (left) and turbulent (right) inflow cases.

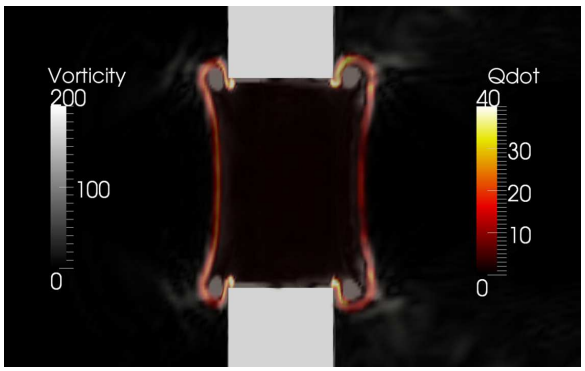

(a) side-cut

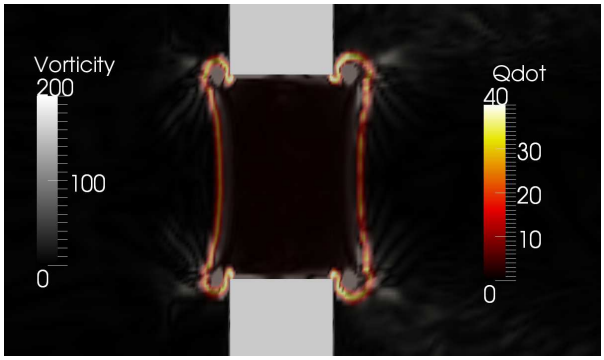

(b) side-cut

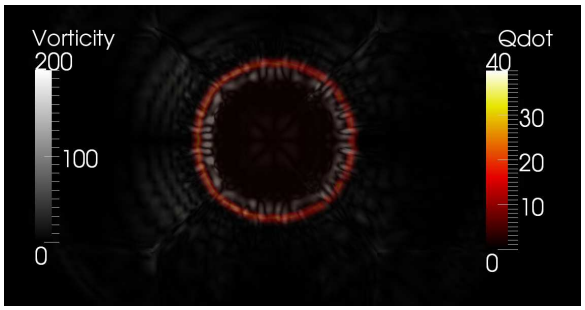

(c) vertical-cut

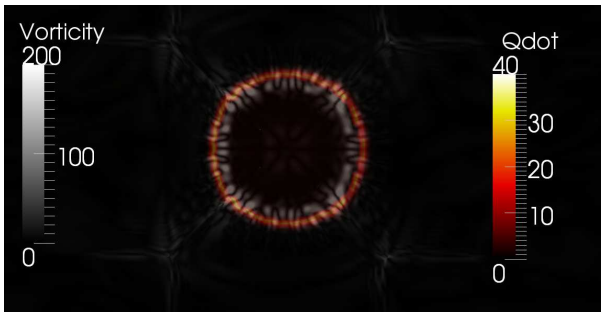

(d) vertical-cut

Fig. 37: $t = 10\mu$**s:** Normalized heat-release and normalized vorticity distribution in centered side-and top-cut planes for the laminar (left) and turbulent (right) inflow cases.

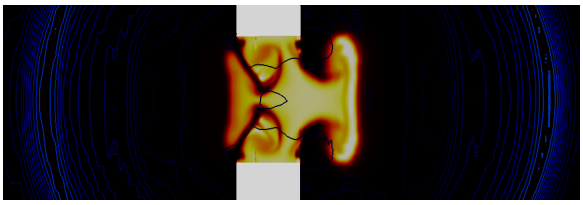

(a) 53μs (side-cut)

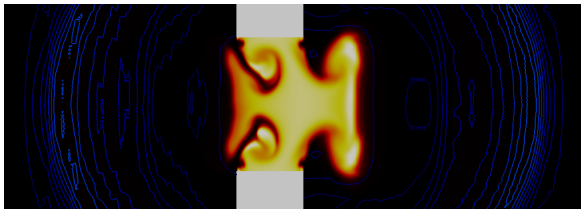

(b) 50μs (side-cut)

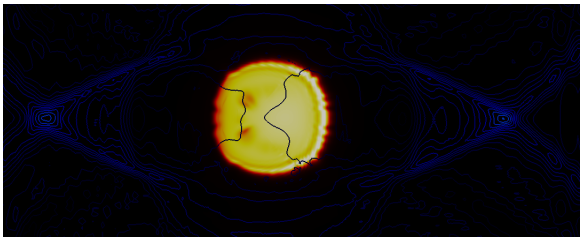

(c) 53μs (vertical-cut)

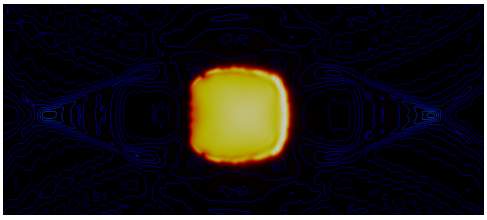

(d) 50μs (vertical-cut)

Fig. 38: $t \sim 50\mu$**s:** Temperature distribution with pressure contours in centered side-and top-cut planes for the laminar (left) and turbulent (right) inflow cases.

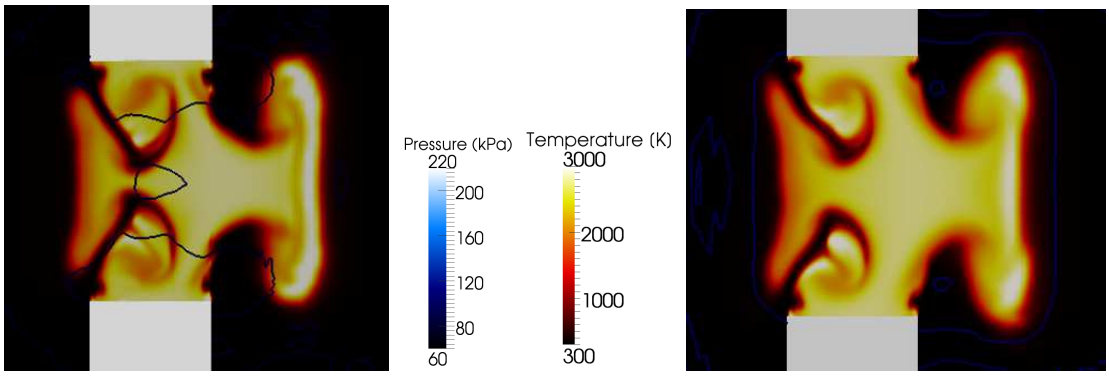

(a) 50μs (side-cut)

(d) 53μs (side-cut)

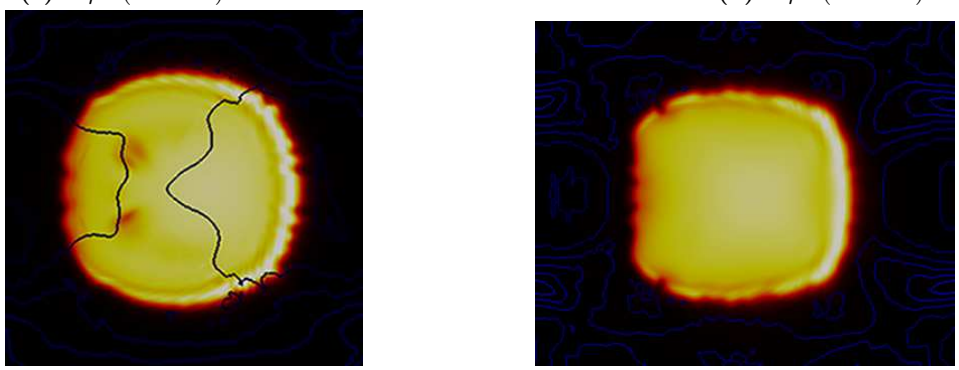

(e) 50μs (vertical-cut)

(f) 53μs u(vertical-cut)

Fig. 39: $t = 10\mu$**s:** Close up of Fig. 38 images.

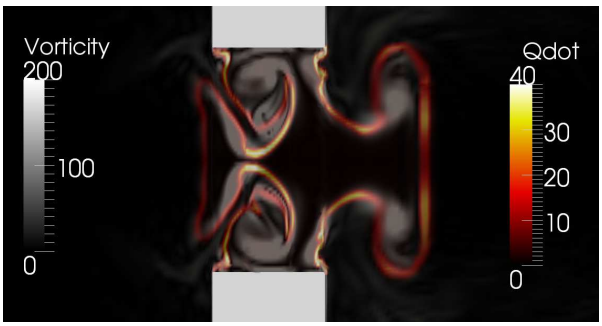

(a) 50μs (side-cut)

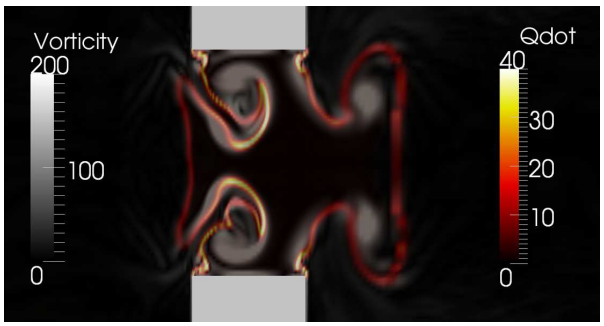

(b) 53μs (side-cut)

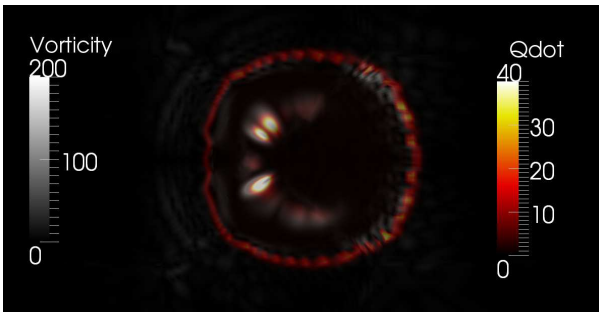

(c) 50μs (side-cut)

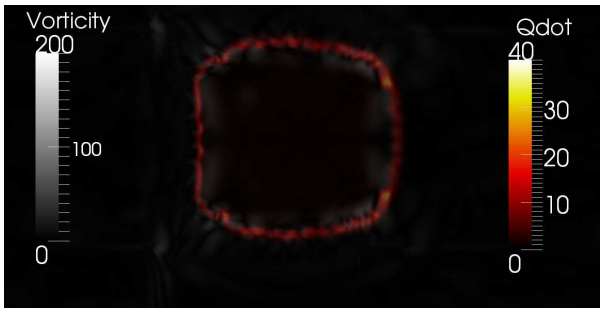

(d) 53μs (side-cut)

Fig. 40: $t \sim 100\mu$**s:** Normalized heat-release and normalized vorticity distribution in centered side- and top-cut planes for the laminar (left) and turbulent (right) inflow cases.

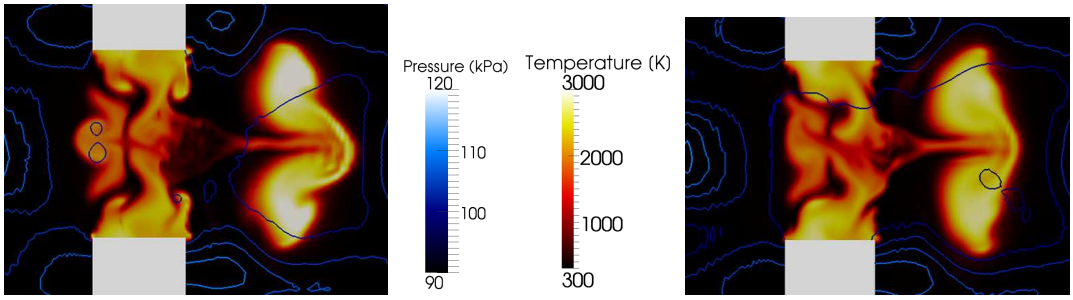

(a) side-cut **(d)** side-cut

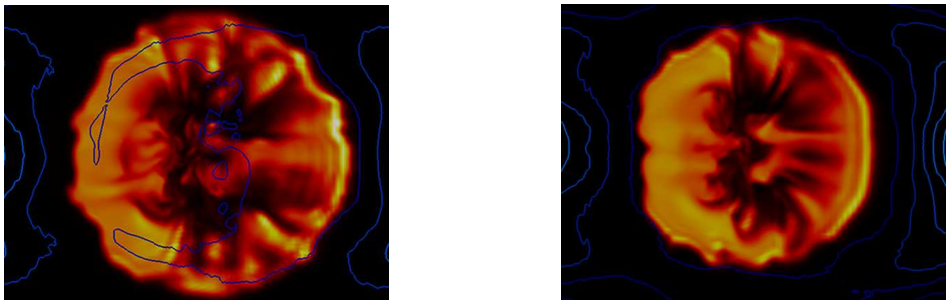

(e) vertical-cut **(f)** vertical-cut

Fig. 41: $t \sim 100\mu$**s:** Temperature distribution with pressure contours in centered side-and top-cut planes for the laminar (left) and turbulent (right) inflow cases.

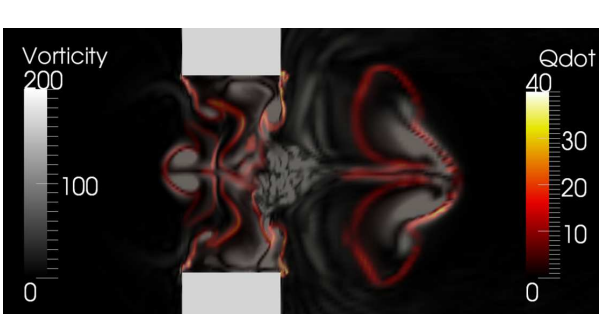

(a) side-cut

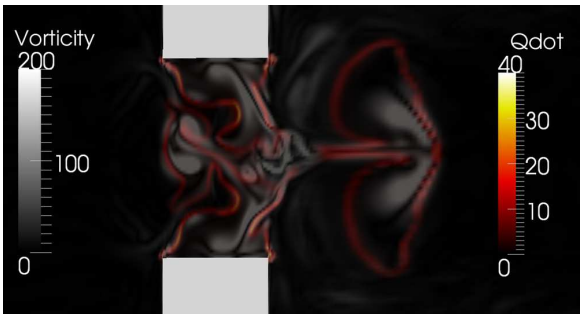

(b) side-cut

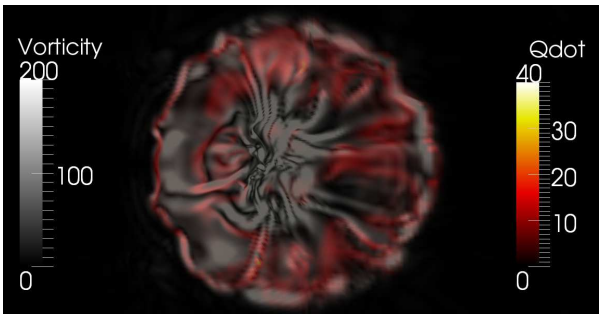

(c) vertical-cut

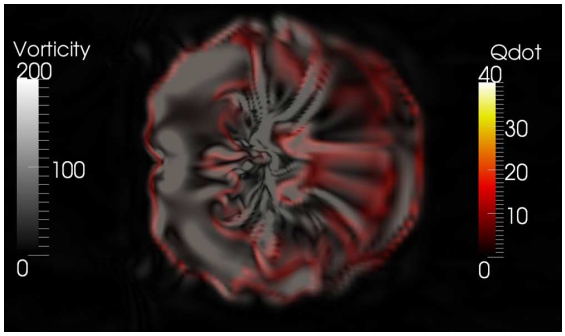

(d) vertical-cut

Fig. 42: $t = 100\mu$**s:** Normalized heat-release and normalized vorticity distribution in centered side- and top-cut planes for the laminar (left) and turbulent (right) inflow cases.

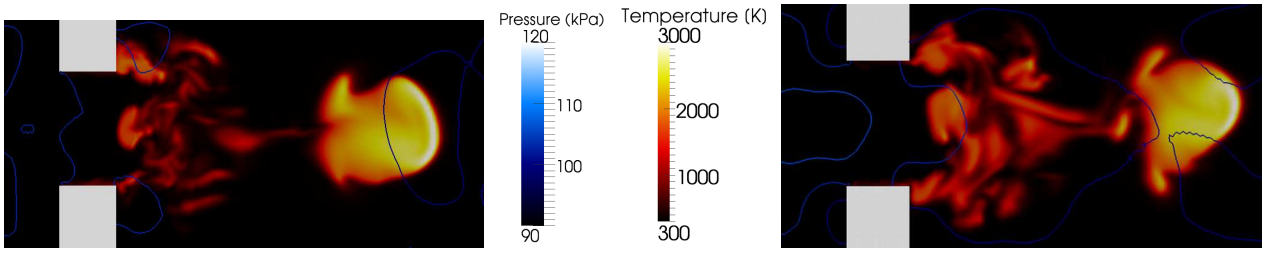

(a) 396μs (side-cut)

(d) 401μs (side-cut)

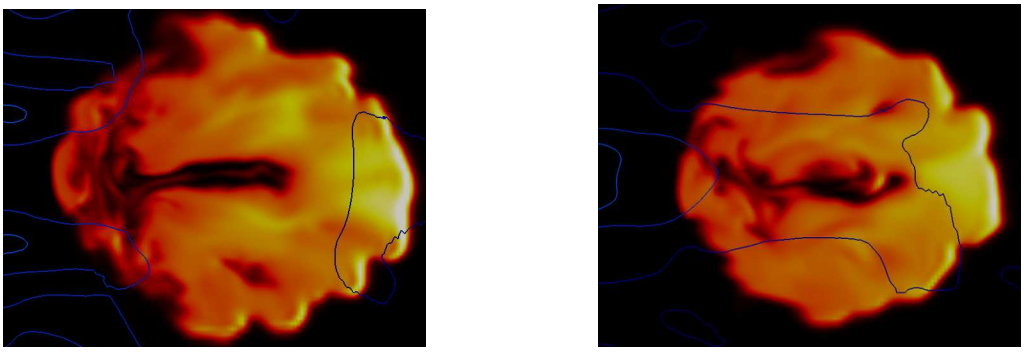

(e) 396μs (vertical-cut)

(f) 401μs (vertical-cut)

Fig. 43: $t = 400\mu$**s:** Temperature distribution with pressure contours in centered side-and top-cut planes for the laminar (left) and turbulent (right) inflow cases.

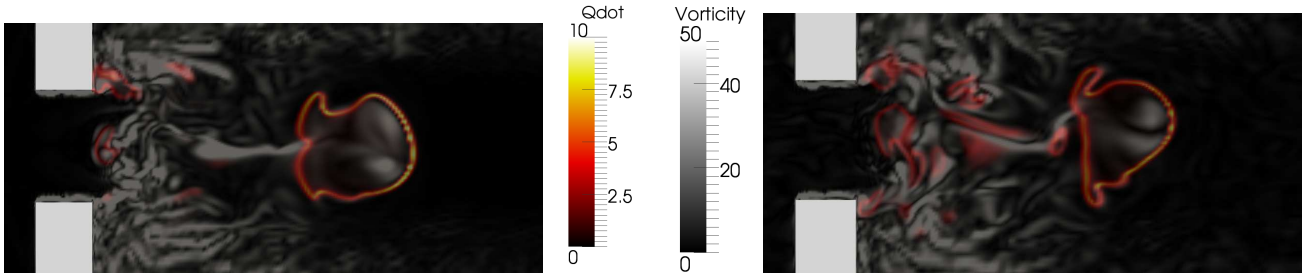

(a) side-cut

(d) side-cut

(e) vertical-cut

(f) vertical-cut

Fig. 44: $t = 400\mu$**s:** Normalized heat-release and normalized vorticity distribution in centered side- and top-cut planes for the laminar (left) and turbulent (right) inflow cases.

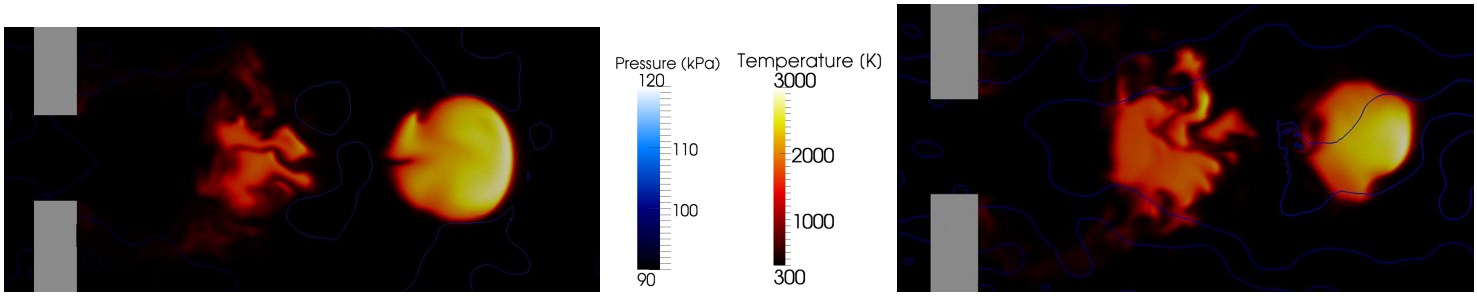

(a) side-cut

(d) side-cut

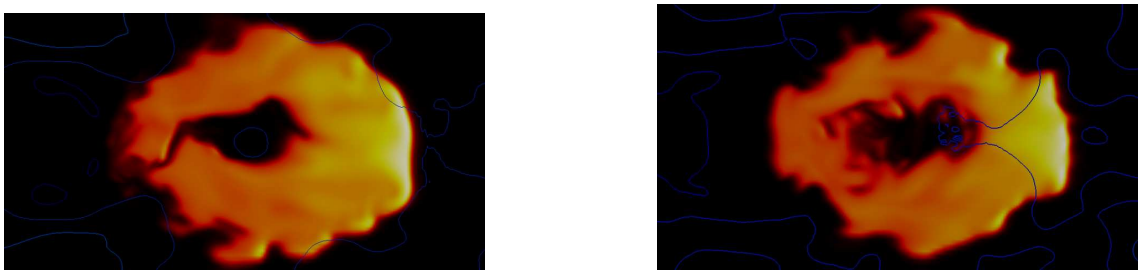

(e) vertical-cut

(f) vertical-cut

Fig. 45: $t = 800\mu$**s:** Temperature distribution with pressure contours in centered side-and top-cut planes for the laminar (left) and turbulent (right) inflow cases.

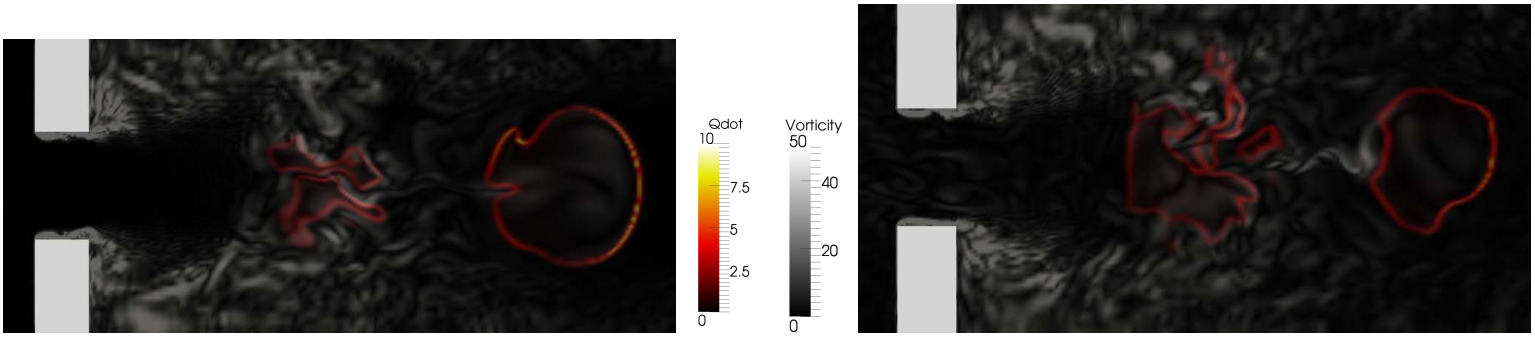

(a) side-cut

(d) side-cut

(e) vertical-cut

(f) vertical-cut

Fig. 46: $t = 800\mu$**s:** Normalized heat-release and normalized vorticity distributions in centered side- and top-cut planes for the laminar (left) and turbulent (right) inflow cases.

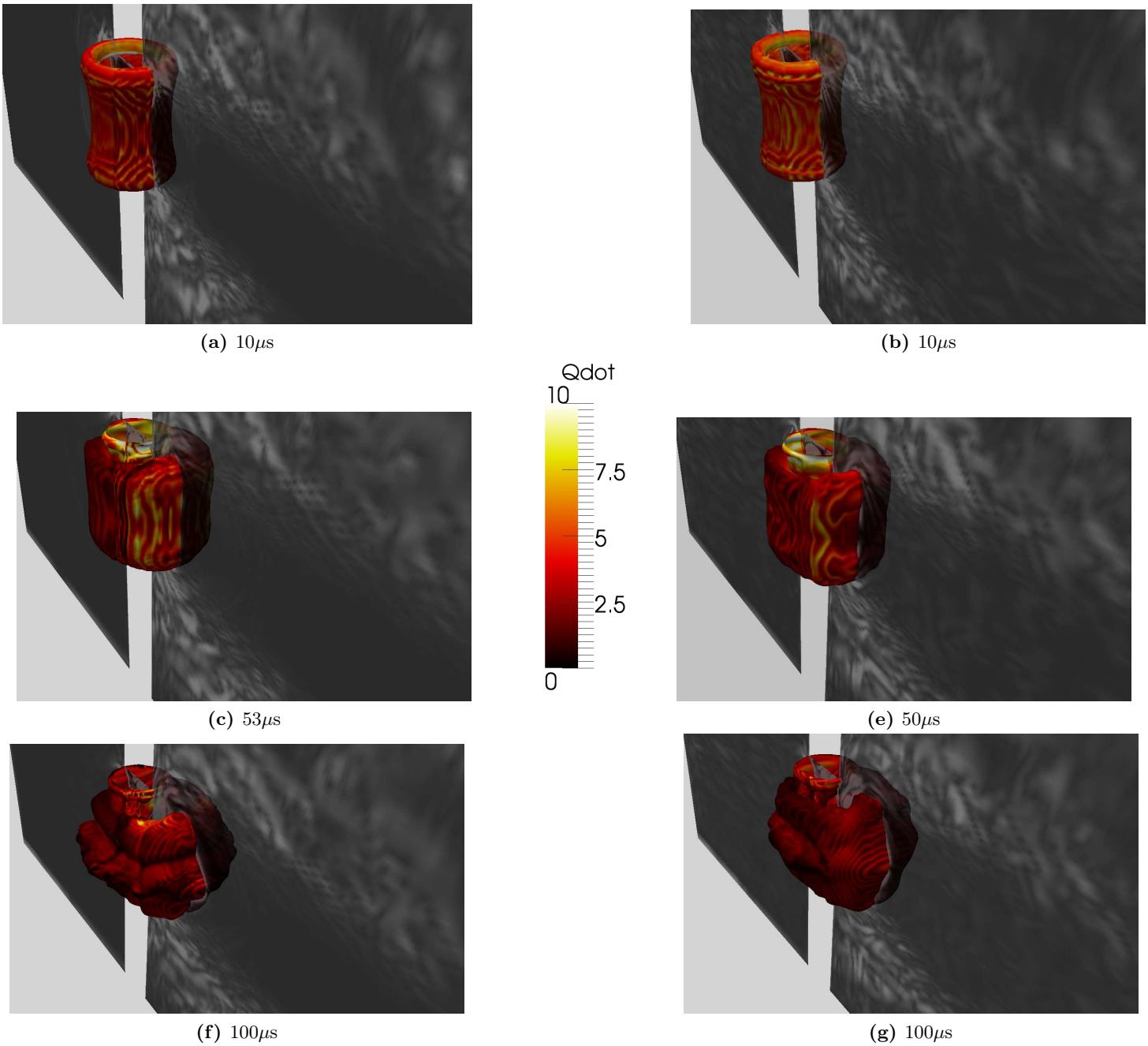

(a) $10\mu s$ **(b)** $10\mu s$

(c) $53\mu s$ **(e)** $50\mu s$

(f) $100\mu s$ **(g)** $100\mu s$

Fig. 47: Angled perspective showing iso-surfaces for $T = 1700K$ colored by normalized heat-release with centered streamwise planar cut colored by vorticity for selected times of the laminar (left) and turbulent (right) inflow cases.

In order to examine the overall behavior of the flame kernels in both cases, the global heat release and fuel consumption are shown in Fig. 49. $\dot{Q}$ has been normalized by the bulk enthalpy of reaction entering the channel through the inlet. Similarly, the fuel consumption

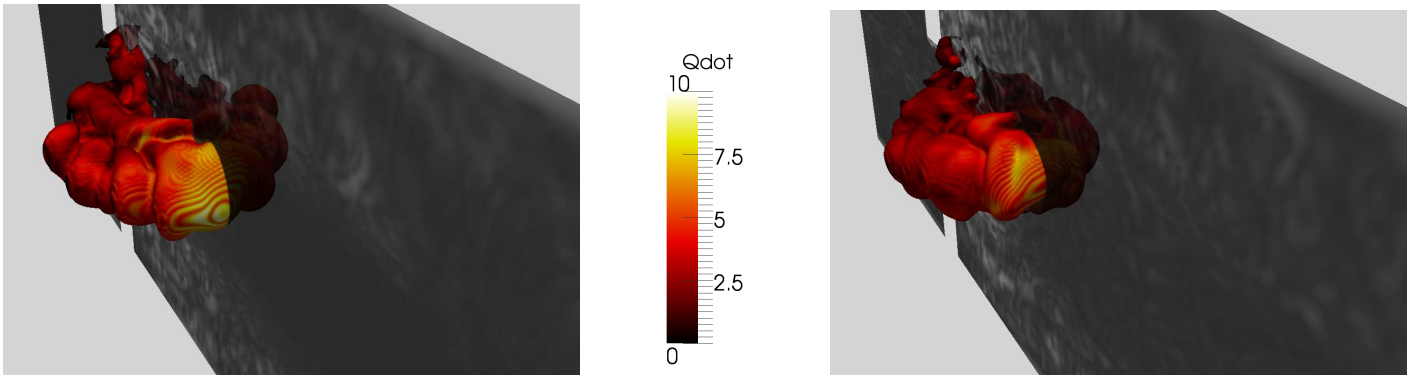

(a) 396μs **(c)** 401μs

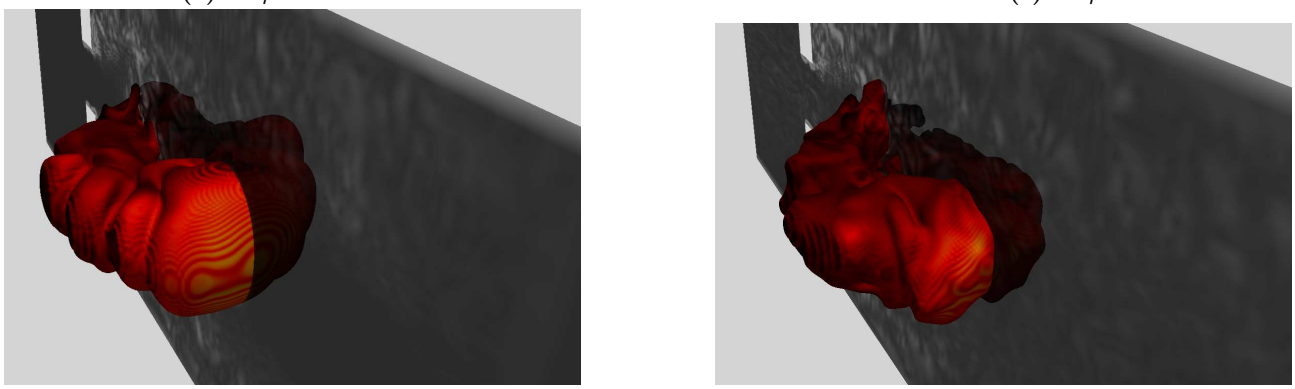

(d) 800μs **(e)** 800μs

Fig. 48: Angled perspective showing iso-surfaces for $T = 1700K$ colored by normalized heat-release with centered streamwise planar cut colored by vorticity for selected times of the laminar (left) and turbulent (right) inflow cases.

has been normalized by the total inflow flux of methane mass. The fuel consumption is essentially correlated with the heat-release. Both cases follow a similar trend in the first 100μs, where there is a sudden drop in heat-release as the temperature quickly decreases due to rapid kernel expansion in the first $\sim$ 20μs. This is quickly recovered as both cases then begin to follow the same rate of increased reaction. Near 170μs, the reaction rate of the turbulent case begins to drop, whereas the the laminar inflow case increases with a delayed drop near 200μs.

Taking a closer look into this sudden change in heat release, the $\dot{Q}$ and $\dot{omega}_{CH_4}$ are examined at 200μs in Fig. 51. It appears that the increase in heat release is largely attributable to an increased packing of the upstream facing side of the downstream core. The flame folding which originated from the outward push given by the entrainment velocities appears to be important in inducing large degrees of negative (concave) flame curvature, causing a

thermodiffusive effect that increases the local heat release. This effect is temporary though, and as the cusps dissappear within $100 - 200\mu$s, the consumption speed decrease. However, the flame recovers quickly and global rates begin to increase as the flamae assumes a more stable shape. Although the turbulent inflow kernel rate values begin to decrease earlier, the recovery appears to occur at a faster pace. This is probably due to the enhanced mixing in the upstream region, increasing the rate of consumption per volume, as seen in Fig. 44 and Fig. 46.

Much of the larger kernel growth in the laminar inflow case can be attributed to the greater amount of hot ($T > 3000K$) fluid in the leading core of the kernel, which helps drive the reaction rates. This stems from an early event shown in Fig. 52. At $t = 20\mu$s, there is very little if any such hot volumes of gas in the kernel. In fact, there appears to be more present in the turbulent inflow case. However, as can be seen for $t = 30\mu$s, a large amount of high-temperature volume forms in the leading edge of the kernel.

The kernel volumes for regions with temperature above a cutoff of $T > 1200K$ are shown in Fig. 54. The kernels appear to increase almost linearly in volume. The turbulent inflow begins to deviate from the steady growth of the laminar inflow near 300μs. This is most likely due to the decrease in the reaction rates mentioned above, since at this point volume being raised in temperature will be due to exothermic combustion reactions. The turbulent inflow volume data stops at 900μs due to lack of data, not extinction or sudden drop in temperature.

The passive scalar mixture fraction distributions are shown for various times in Fig. 53 for the turbulent inflow case. We see that for the first 10μs microseconds, the initial rapid expansion simply pushes much of the cold fluid aside, and only begins to entrain the reactants near the electrodes. At 50μs, it appears that already a large degree of mixing has taken place during the entrainment on the upstream end. At the leading lobe, there is yet further evidence of mixing into this portion of the kernel. Although the kernel has broken off and has formed a toroidal shape by $t = 100\mu$s, there are still large pockets of unmixed fluid within

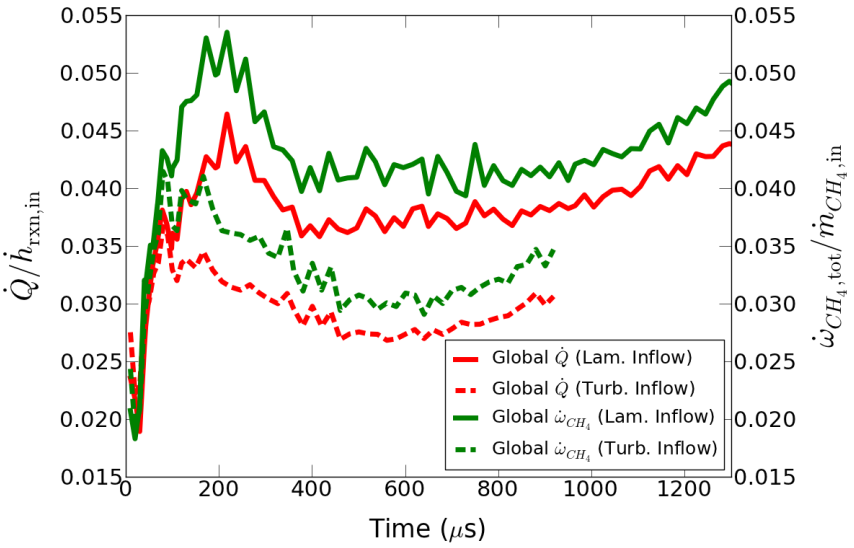

Fig. 49: Plot of time-variation in global normalized heat-release and fuel consumption for both laminar and inflow cases. Note that the data in the turbulent inflow case is limited to $t < 918\mu$s.

the kernel. By $t = 300\mu$s, much of the kernel has mixed with a mixture fraction distribution that is becoming increasingly more uniform within the kernel volume.

The plot in Fig. 54 presents the kernel volume for various cut-off temperatures, as well as the average mixture fraction within the specified kernel normalized by the initial concentration of passive scalar marker in the ambient fluid. As before, the kernel volume, after an initial jump due to the shock-expansion, increases fairly linearly for most temperatures. The limiting value of $T > 2400K$ is approximately the minimal temperature below which the kernel volumes were seen to grow. All volumes for $T > 2400K$ decreased fairly quickly after the initial expansion. This is due to the fact that the cooling of the hot regions is faster than the net heating due to the chemical reactions. Evidently, as the cut-off temperature decreases the kernel volume is seen to increase for a given time. This is because the direction of heat diffusion is towards the cold regions, causing colder volumes to heat up more rapidly. In order to quantify the effects of heat-release, a non-reacting case was run up to 50μs for the purpose of comparison. Although the cut-off temperature was selected as $1200K$, the volume is seen to decrease immediately after the initial 1μs expansion, whereas the reacting $T > 1200K$ is

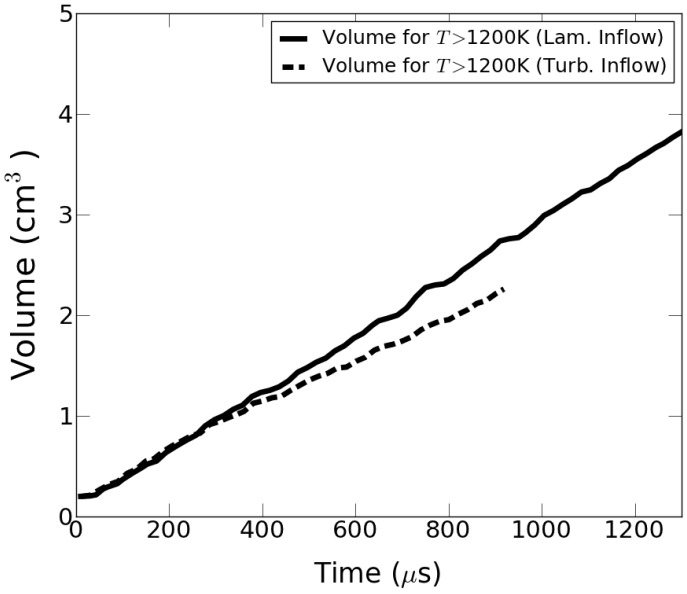

Fig. 50: Plot of time-variation in total volume for a selected cut-off temperature of $T_{lim} = 1200K$ for both laminar and inflow cases. Note that the data in the turbulent inflow case is limited to $t < 918\mu$s.

seen to increase at this early time. This is yet further evidence of reactions governing the kernel-dynamics very early on in the simulation.

Also shown on the plot in Fig. 54 is the average mixture fraction of the passive scalar introduced in the initialization. As the marker concentration was inserted somewhat arbitrarily in regions where $T < 1000K$, the value of Y_{mark} is zero in volumes of high temperature ($T > 2400K$) since it takes some time for the marker to mix into these volumes. The mixing process in this case is also competing with the shrinking of the kernel volume as these regions cool down, which justifies why there is such a long period of time before the mixture fraction is seen to increase ($\sim 40\mu$s. As for the colder cut-off temperatures, the entrainment process increases Y_{mark} for $T > 1200K$ and $T > 1700K$ at $t \sim 1\mu$s. The coldest case of $T > 600$ actually begins with a marker concentration, which is why it is seen to spike up so rapidly. The mixture fraction values are generally seen to increase fairly quickly for the first 90μs before slowly approaching unity. This initial slope is mainly due to the principal entrainment period, which finishes when the kernel pinches off between opposing sides in the center and

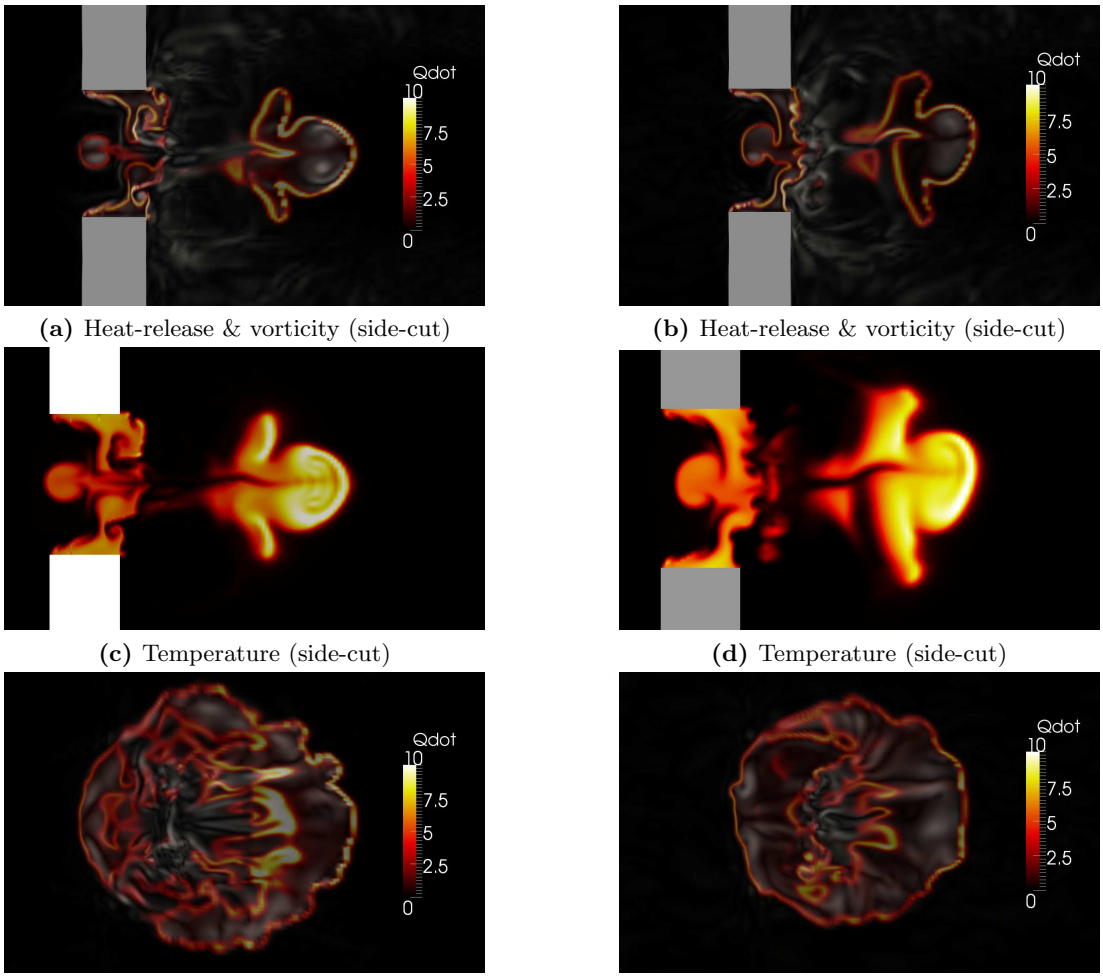

(a) Heat-release & vorticity (side-cut)

(b) Heat-release & vorticity (side-cut)

(c) Temperature (side-cut)

(d) Temperature (side-cut)

(e) Heat-release & vorticity (vertical-cut)

(f) Heat-release & vorticity (vertical-cut)

Fig. 51: $t = 200\mu$**s:** Centered side- and vertical-cut planes of normalized heat-release, vorticity and temperature distributions for the laminar (left) and turbulent (right) inflow cases.

begins folding in on itself on the downstream side. As the kernel continues to evolve, most of the increase in mixture fraction is then attributable to the increase in flame volume due to propagation of flame fronts and the diffusion processes involved.

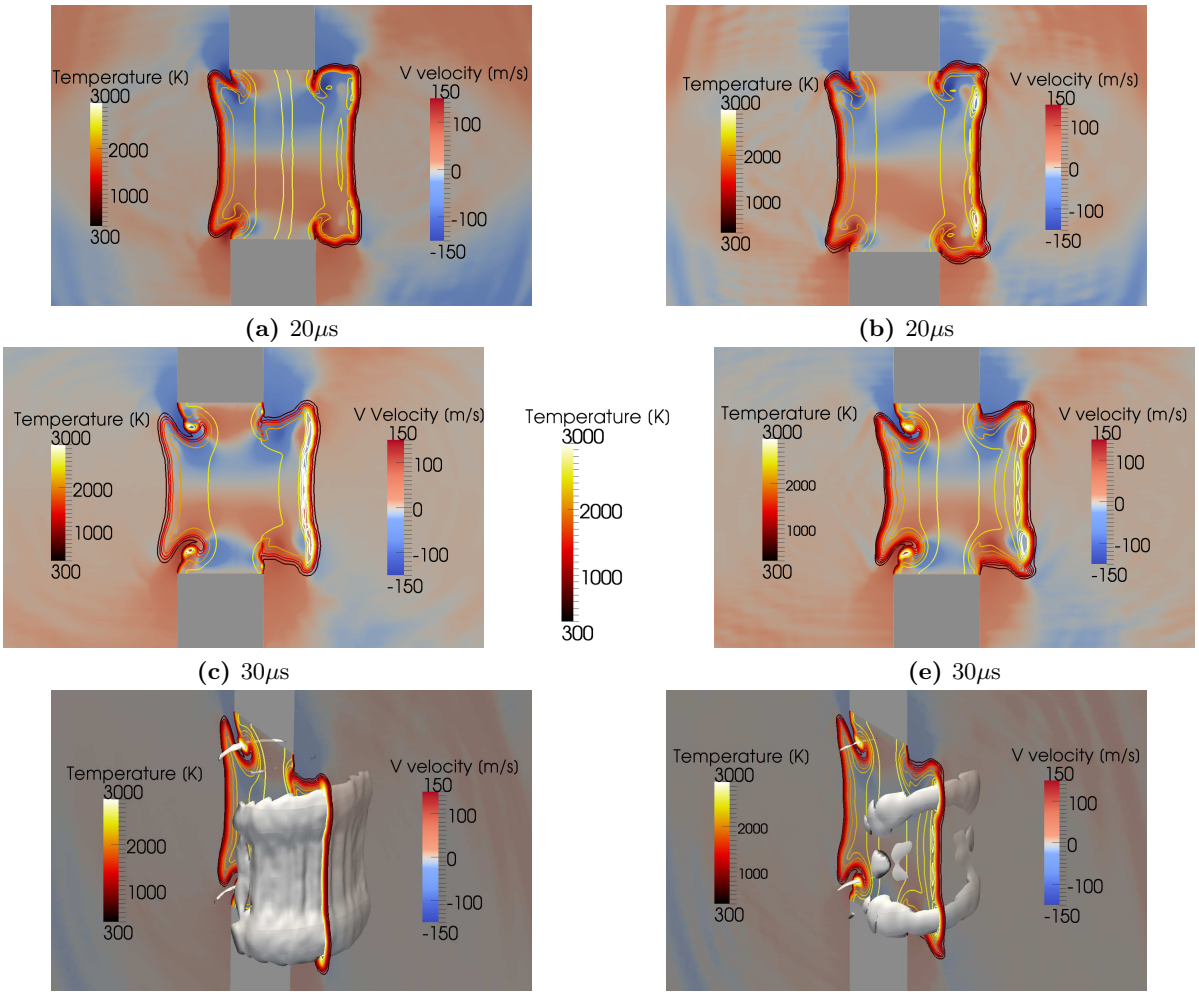

(a) $20\mu s$ **(b)** $20\mu s$

(c) $30\mu s$ **(e)** $30\mu s$

(f) $30\mu s$ **(g)** $30\mu s$

Fig. 52: Centered vertical velocity distributions in side-cut planes for selected times in (a), (b), **(c)**, (d). Shown also in (f) and (g) are the iso contours for $T = 3000K$ with centered side-cut plane colored by vertical velocity. Shown are the laminar (left) and turbulent (right) inflow cases.

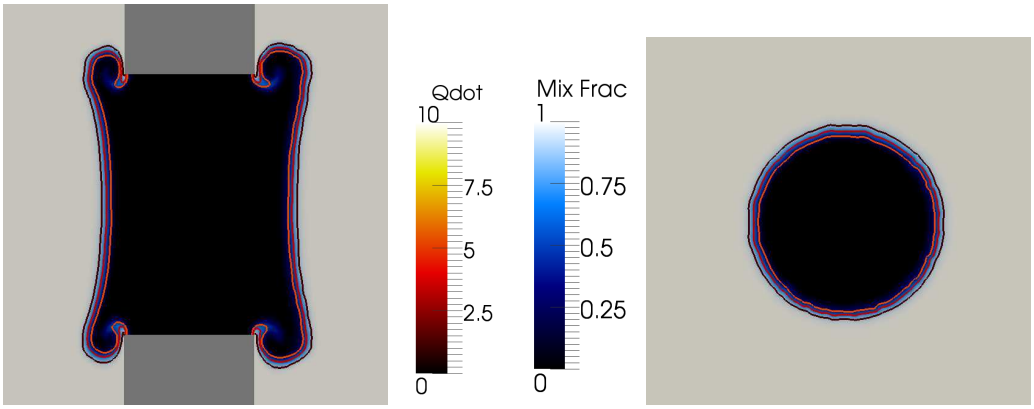

(a) 10μs (side-cut)

(d) 10μs (vertical-cut)

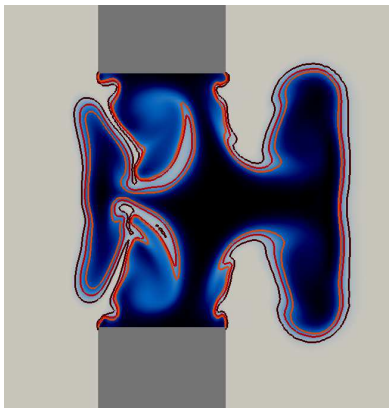

(e) 50μs (side-cut)

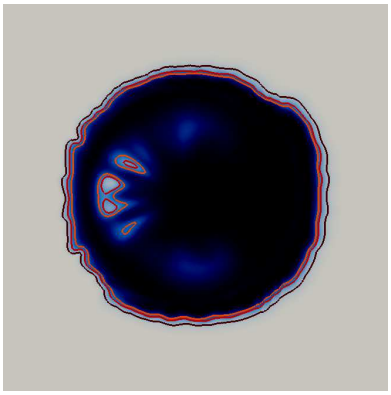

(f) 50μs (vertical-cut)

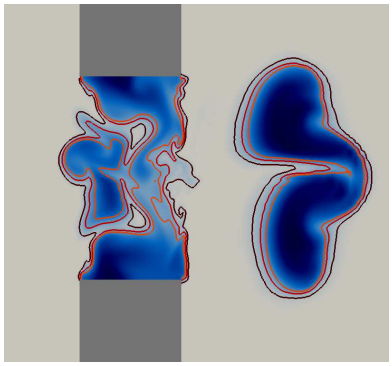

(g) 100μs (side-cut)

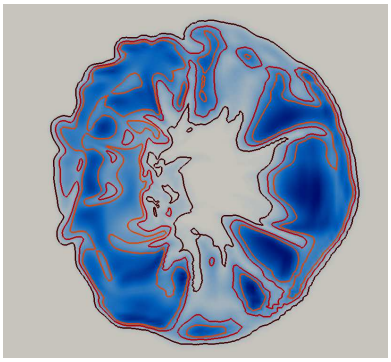

(h) 100μs (vertical-cut)

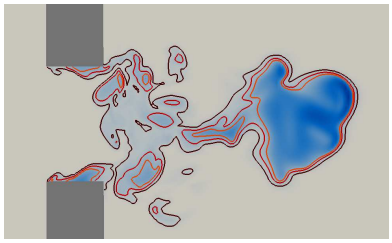

(i) 300μs (side-cut)

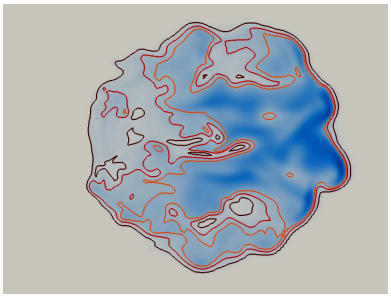

(j) 300μs (vertical-cut)

Fig. 53: Mixture fraction distribution and temperature contours of T =600K, 1200K, and 1700K in centered side- and -vertical cut planes for the turbulent inflow case only.

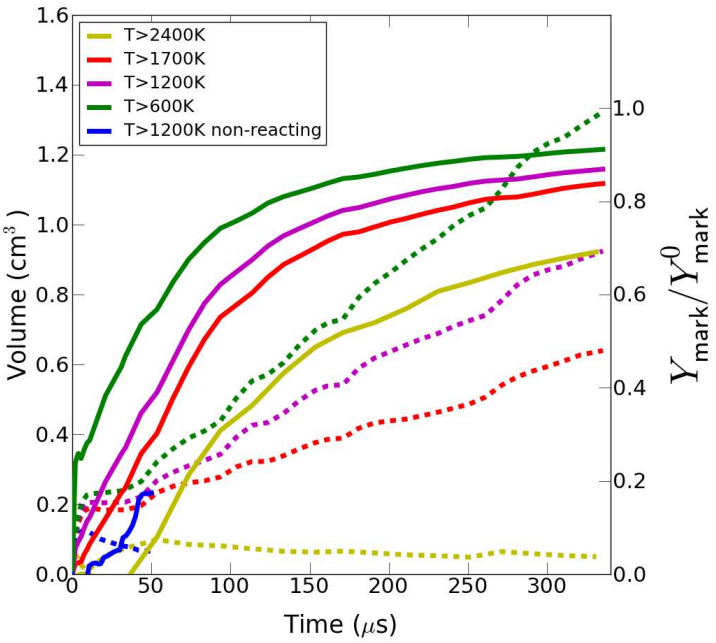

Fig. 54: Plot of time variation in total volume and normalized average mixture fraction for regions of temperature over various cut-off values. Shown for turbulent case only. Data for non-reacting case is limited to $t < 50\mu$s.

6 Conclusion

6.1 Spherical Turbulent Flame

- For similar charateristic lengthscales, the distribution of turbulent energy can still have large effects on flame wrinkling, flame speed and spherical flame growth.
- The size of the grid domain is important in preserving the isotropic quality of turbulence in the unburned mixture, even if the integral lengthscale is much smaller than the domain size ($\sim 10\%$).
- Overall, the effects of turbulence on the development of spherical flames can be simulated using LES without a turbulent mixing cloure. This is true for fine grids which at least resolve the flame front and for turbulent intensities within the flamelet regime.

6.2 Spark Ignition in a Channel

- Reactions occur almost immediately, causing large amounts of heat-release for $t < 1\mu$s
- The ignition process occurs in a series of stages:
  1. $0 - 1\mu$s: Spark kernel expansion
  2. $1 - 100\mu$s: Entrainement and kernel pinching; toroid formation
  3. $100 - 200\mu$s: Kernel separation; flame-driven growth
  4. $200 - ...\mu$s: Continued flame propagation
- High thermal energy from spark persists in flame for long times (up to $t \sim$ms) and helps drive flame growth.
- The net effect of turbulence actually decreases the overall heat-release rate in the first $\sim$1ms.
- Coherent vortical structures within the kernel persist until at least 1ms, and contribute to internal mixing.

- Although previous studies have shown that turbulent effects are typically felt near 100μs, it is seen that early minor deviations in flow structure can lead to different flame dynamics at earlier times.

- The presence of electrodes as well as mean flow velocity results in flame kernel development that deviates significantly from spherical flame development. This is due to flow interaction with the electrode geometery that is anti-symmetric in the electrode axis , which results in flame structure that is markedly different between up and downstream sides of the produced flame.

8 Appendix

8.1 Appendix A: Spark Kernels in Air

Before introducing premixed fuel into the problem, it was first beneficial to examine a spark formed in air only. This would serve as a preliminary feasibility study in modelling spark kernel formation, and in so doing help elucidate the role of heating and ionization in the problem. This could then also be used as a basis for comparison between fuel/air cases, and allow the effect of combustion chemistry to be better understood once it was introduced.

As in the CH_4/air simulations, an opposing-electrode geometry with the same dimensions was used, since the apparatus for the experiment remained the same. A grid was developed using the Gridgen meshing software, and contained similar stretching and O-grid features to the mesh described in the main body of this document.

No-slip boundary conditions were imposed on the walls. A subsonic non-reflective condition was used at the inflow, where a laminar stream with mean velocity of 33m/s was

prescribed to match experiment. A subsonic non-reflective outflow with sponge-averaging was also used.

In order to include the effects of ionization, chemistry was calculated with a 30-step/11-species high-temperature air mechanism [34]. The second-order Euler scheme was used for integration. The Hybrid scheme was used for flow calculations, with subgrid terms being closed with dynamic LES.

The ambient air was set at $T = 300K$ and $P = 1$atm. The initial spark kernel was defined as a cylindrical volume containing a uniform spark energy density, as before. It was assumed that the time-scale of energy deposition and kernel formation was much smaller than that of the flow, and that the resulting kernel was in thermal and chemical equilibrium. This assumption was based on previous constant-volume calculations [21] which indicated that equilibrium was reached on the order of 1μs. The composition of the spark was determined by equilibrium calculations for a specified energy density using NASA CEA. Unlike the methane/air kernel, however, the plasma-air spark was inserted as a delta-function without a prescribed Gaussian distribution. This avoided the problem of determining how to prescribe a continuous chemistry and temperature profile for the kernel which matched a given energy density distribution (note that this was not an issue for the CH_4/air case, since the specific heat was held constant and only the temperature distribution needed to be defined). The gradient was therefore imposed with a width equal to the local cell size of $\approx 30\mu$m.

A total spark energy of 0.25J was chosen to approximate the readings found in experiment. The effect of initial spark volume, and therefore energy density, was determined by varying the initial spark diameter. The spark properties were therefore calculated using diameters of 0.8mm, 1.0mm, and 1.2mm, which resulted in temperatures ranging from 9592K to 17772K.

References

[1] RG Abdel-Gayed and D. Bradley. Criteria for turbulent propagation limits of premixed flames. *Combustion and flame*, 62(1):61–68, 1985.

[2] OO Akindele, D. Bradley, PW Mak, and M. McMahon. Spark ignition of turbulent gases. *Combustion and Flame*, 47:129–155, 1982.

[3] DR Ballal and AH Lefebvre. Ignition and flame quenching in flowing gaseous mixtures. *Proceedings of the Royal Society of London. A. Mathematical and Physical Sciences*, 357(1689):163–181, 1977.

[4] JH Bechtel, R.J. Blint, C.J. Dasch, and D.A. Weinberger. Atmospheric pressure premixed hydrocarbon-air flames: Theory and experiment. *Combustion and Flame*, 42:197–213, 1981.

[5] D. Bradley and F.K.K. Lung. Spark ignition and the early stages of turbulent flame propagation. *Combustion and flame*, 69(1):71–93, 1987.

[6] N. Chakraborty, M. Klein, and RS Cant. Stretch rate effects on displacement speed in turbulent premixed flame kernels in the thin reaction zones regime. *Proceedings of the Combustion Institute*, 31(1):1385–1392, 2007.

[7] GG De Soete. Fifteenth symposium (international) on combustion. *The Combustion Institute, Pittsburgh*, page 1093, 1975.

[8] A. Dreizler, S. Lindenmaier, U. Maas, J. Hult, M. Aldén, and CF Kaminski. Characterisation of a spark ignition system by planar laser-induced fluorescence of oh at high repetition rates and comparison with chemical kinetic calculations. *Applied Physics B: Lasers and Optics*, 70(2):287–294, 2000.

[9] J.F. Driscoll. Turbulent premixed combustion: Flamelet structure and its effect on turbulent burning velocities. *Progress in Energy and Combustion Science*, 34(1):91–134, 2008.

[10] K. Eisazadeh-Far, F. Parsinejad, H. Metghalchi, and J.C. Keck. On flame kernel formation and propagation in premixed gases. *Combustion and Flame*, 157(12):2211–2221, 2010.

[11] B. Enaux, V. Granet, O. Vermorel, C. Lacour, C. Pera, C. Angelberger, and T. Poinsot. Les study of cycle-to-cycle variations in a spark ignition engine. *Proceedings of the Combustion Institute*, 33(2):3115–3122, 2011.

[12] J. Ewald and N. Peters. On unsteady premixed turbulent burning velocity prediction in internal combustion engines. *Proceedings of the Combustion Institute*, 31(2):3051–3058, 2007.

[13] A. Eyssartier, B. Cuenot, LYM Gicquel, and T. Poinsot. Using les to predict ignition sequences and ignition probability of turbulent two-phase flames. *Combustion and Flame, submitted to*, 2011.

[14] G. Fru, D. Thévenin, and G. Janiga. Impact of turbulence intensity and equivalence ratio on the burning rate of premixed methane–air flames. *Energies*, 4(6):878–893, 2011.

[15] S. Gashi, J. Hult, K.W. Jenkins, N. Chakraborty, S. Cant, and C.F. Kaminski. Curvature and wrinkling of premixed flame kernels–comparisons of oh plif and dns data. *Proceedings of the Combustion Institute*, 30(1):809–817, 2005.

[16] DG Goodwin. An open-source, extensible software suite for cvd process simulation. *Chemical Vapor Deposition XVI and EUROCVD*, 14(2003):08, 2003.

[17] V. Granet, O. Vermorel, C. Lacour, B. Enaux, V. Dugué, and T. Poinsot. Large-eddy simulation and experimental study of cycle-to-cycle variations of stable and unstable operating points in a spark ignition engine. *Combustion and Flame*, 2011.

[18] GRA Groot and LPH De Goey. A computational study on propagating spherical and cylindrical premixed flames. *Proceedings of the Combustion Institute*, 29(2):1445–1451, 2002.

[19] XJ Gu, MZ Haq, M. Lawes, and R. Woolley. Laminar burning velocity and markstein lengths of methane–air mixtures. *Combustion and flame*, 121(1):41–58, 2000.

[20] CF Kaminski, XS Bai, J. Hult, A. Dreizler, S. Lindenmaier, and L. Fuchs. Flame growth and wrinkling in a turbulent flow. *Applied Physics B: Lasers and Optics*, 71(5):711–716, 2000.

[21] J. Kim, B. Sforzo, and V.R. Pasumarti. *Pratt & Whitney C.O.E. Georgia Tech Review Presentation*, 2010.

[22] M. Kono, K. Niu, T. Tsukamoto, and Y. Ujiie. Mechanism of flame kernel formation produced by short duration sparks. In *Symposium (International) on Combustion*, volume 22, pages 1643–1649. Elsevier, 1989.

[23] R.H. Kraichnan. Diffusion by a random velocity field. *Physics of Fluids*, 13(1):22–31, 1970.

[24] T. Kravchik and E. Sher. Numerical modeling of spark ignition and flame initiation in a quiescent methane-air mixture. *Combustion and flame*, 99(3-4):635–643, 1994.

[25] G. Lacaze, B. Cuenot, T. Poinsot, and M. Oschwald. Large eddy simulation of laser ignition and compressible reacting flow in a rocket-like configuration. *Combustion and Flame*, 156(6):1166–1180, 2009.

[26] G. Lacaze, E. Richardson, and T. Poinsot. Large eddy simulation of spark ignition in a turbulent methane jet. *Combustion and Flame*, 156(10):1993–2009, 2009.

[27] MT Lim, RW Anderson, and V.S. Arpaci. Prediction of spark kernel development in constant volume combustion. *Combustion and flame*, 69(3):303–316, 1987.

[28] R. Maly. Ignition model for spark discharges and the early phase of flame front growth. In *Symposium (International) on Combustion*, volume 18, pages 1747–1754. Elsevier, 1981.

[29] R. Maly and M. Vogel. Initiation and propagation of flame fronts in lean ch4-air mixtures by the three modes of the ignition spark. In *Symposium (International) on Combustion*, volume 17, pages 821–831. Elsevier, 1979.

[30] N. Peters. *Turbulent combustion*. Cambridge Univ Pr, 2000.

[31] B. Renou, A. Boukhalfa, D. Puechberty, and M. Trinité. Local scalar flame properties of freely propagating premixed turbulent flames at various lewis numbers. *Combustion and Flame*, 123(4):507–521, 2000.

[32] S. Richard, O. Colin, O. Vermorel, A. Benkenida, C. Angelberger, and D. Veynante. Towards large eddy simulation of combustion in spark ignition engines. *Proceedings of the Combustion Institute*, 31(2):3059–3066, 2007.

[33] R. Sankaran, E.R. Hawkes, J.H. Chen, T. Lu, and C.K. Law. Structure of a spatially developing turbulent lean methane–air bunsen flame. *Proceedings of the combustion institute*, 31(1):1291–1298, 2007.

[34] JC Schulz, KC Gottiparthi, and S. Menon. Ionization in gaseous detonation waves. *Shock Waves*, pages 1–12, 2012.

[35] E. Sher, J. Ben-Ya'ish, and T. Kravchik. On the birth of spark channels. *Combustion and flame*, 89.

[36] SM Starikovskaia. Plasma assisted ignition and combustion. *Journal of Physics D: Applied Physics*, 39:R265, 2006.

[37] D. Thévenin. Three-dimensional direct simulations and structure of expanding turbulent methane flames. *Proceedings of the Combustion Institute*, 30(1):629–637, 2005.

[38] M. Thiele, S. Selle, U. Riedel, J. Warnatz, and U. Maas. Numerical simulation of spark ignition including ionization. *Proceedings of the combustion institute*, 28(1):1177–1185, 2000.

[39] C.M. Vagelopoulos and F.N. Egolfopoulos. Direct experimental determination of laminar flame speeds. In *Symposium (international) on combustion*, volume 27, pages 513–519. Elsevier, 1998.

[40] O. Vermorel, S. Richard, O. Colin, C. Angelberger, A. Benkenida, and D. Veynante. Towards the understanding of cyclic variability in a spark ignited engine using multi-cycle les. *Combustion and Flame*, 156(8):1525–1541, 2009.

[41] G. Wang, M. Boileau, D. Veynante, and K. Truffin. Large eddy simulation of a growing turbulent premixed flame kernel using a dynamic flame surface density model. *Combustion and Flame*, 2012.

[42] G.F.W. Ziegler, E.P. Wagner, and R.R. Maly. Ignition of lean methane-air mixtures by high pressure glow and arc discharges. In *Symposium (International) on Combustion*, volume 20, pages 1817–1824. Elsevier, 1985.